

Conductivity and scattering Q in GPR data: Example from the Ellenburger dolomite, central Texas

Hussein Harbi¹ and George A. McMechan²

ABSTRACT

Total attenuation (Q_t^{-1}) in ground-penetrating radar (GPR) data is a composite of intrinsic and scattering attenuations (Q_{in}^{-1} and Q_{sc}^{-1}). For nonmagnetic materials, Q_{in}^{-1} is a combination of the effects of real conductivity and dielectric relaxation. The attenuation for real conductivity >1.0 mS/m in the GPR frequency band is a function of frequency while the dielectric relaxation is frequency-independent. These frequency behaviors allow separation of the attenuation types by attributing and fitting the Q_t^{-1} decay shape with frequency to the conductivity, and by attributing the magnitude of Q_t^{-1} to the sum of conductivity and dielectric relaxation attenuations at each frequency. Total attenuation is calculated from GPR data using spectral ratios, and Q_{in}^{-1} is obtained by fitting a smooth lower bound to Q_t^{-1} ; the difference between Q_t^{-1} and Q_{in}^{-1} estimates the scattering contribution Q_{sc}^{-1} . Scatterer size spectra are evaluated using

$KA = 1$ for 2D, and $KA = 1.5$ for 3D, propagation (where K is wavenumber and A is the scatterer size). We illustrate with 2D synthetic data and three field 2D crosshole profiles from an outcrop of an Ellenburger collapsed paleocave environment in central Texas. Between the three pairs of holes, we estimate the breccia sizes from the scattering spectra Q_{sc}^{-1} . To image the anisotropic electrical conductivity distributions, we use simultaneous iterative reconstruction tomography. There is a correlation between the low wavenumber features of the results of the current conductivity tomography and those in previous velocity tomography, and with surface data results that are predicted and calculated from GPR data attributes. Low- and high-conductivity zones tend to follow either the GPR facies distributions, lithological boundaries, or the larger of the fractures. Correlations are not visible where the breccias are finer because these tend to be more randomly oriented, and/or below the resolution of the GPR data.

INTRODUCTION

Velocity and attenuation in GPR data are determined by the dielectric permittivity, magnetic permeability, and the electrical conductivity; all are complex and frequency-dependent (Keller, 1987; Turner and Siggins, 1994; Bradford, 2007; Giroux and Chouteau, 2010). High-resolution crosshole GPR velocity and attenuation tomography are extensively used in characterizing shallow subsurface aquifers (Tronicke et al., 2004; Bachrach and Mukerji, 2005), reservoir analogs (Hammon III et al., 2002; Harbi and McMechan, 2011), monitoring hydrologic processes (Chang et al., 2004; Schmalholz et al., 2004; Hanafy and Hagrey, 2006; Deiana et al., 2008), fracture imaging (Kowalsky et al., 2005; Zhou et al., 2005;

Liu, 2006), and monitoring subsurface contamination (Cassidy, 2008).

Attenuation and velocity give different information about the lithology and electrical property distributions, and do not have to present the same geometrical distribution (Zhou et al., 2001), although they often do. The dielectric permittivity distribution from a velocity model can be used to map the water content (Topp et al., 1980; Greaves et al., 1996), to estimate porosity (Wharton et al., 1980; Koesoemadinata and McMechan, 2003; Tronicke et al., 2004), and to correlate to the bulk density distribution (Parkhomenko, 1967; Keller, 1987; Guéguen and Palciauskas, 1994; Koesoemadinata and McMechan, 2003). Conductivity distributions, from attenuation measurements, are sensitive to clay content (Giroux and Chouveau, 2004) and to the water content (Davis and Annan, 1989),

Manuscript received by the Editor 8 September 2011; revised manuscript received 12 February 2012; published online 27 June 2012.

¹Formerly The University of Texas at Dallas, Center for Lithospheric Studies, Richardson, Texas, USA; presently King Abdulaziz University, Faculty of Earth Science, Department of Geophysics, Jeddah, Saudi Arabia. E-mail: hharbil@kau.edu.sa.

²The University of Texas at Dallas, Center for Lithospheric Studies, Richardson, Texas, USA. E-mail: mcmec@utdallas.edu.

© 2012 Society of Exploration Geophysicists. All rights reserved.

which correlate to the porosity and fluid permeability distributions (Oldenborger et al., 2007).

In GPR attenuation tomography, the total attenuation is a composite of intrinsic and scattering contributions, but often is approximated by attributing it to only the conductivity (Zhou and Fullagar, 2001; Chang et al., 2004; Schmalholz et al., 2004; Hanafy and Hagrey, 2006). In GPR surveys, increasing the frequency to maximize resolution also increases scattering from small-scale heterogeneities (Davis and Annan, 1989). Takahashi et al. (2011) use geostatistics and a Mie scattering model to investigate GPR scattering in heterogeneous soils. When scattering attenuation is present, errors in estimating electrical properties from the total attenuation increase (Giroux and Chouteau, 2010). Intrinsic and scattering attenuations give independent information about the structure (from scattering) and the lithology (from the intrinsic attenuation) (Kneib and Shapiro, 1995). Intrinsic attenuation of electromagnetic (EM) waves is the result of the real conductivity, and the magnetic permeability and dielectric permittivity relaxation mechanisms (Keller, 1987; Davis and Annan, 1989; Olhoeft and Capron, 1994; Xu and McMechan, 1997).

Estimating and separating intrinsic and scattering Q^{-1} s in surface seismic data often use the amplitude decay of direct arrivals of the P- and S-waves (Kang and McMechan, 1994) and measurements of the coda of scattered waves (e.g., Yomogida and Benites, 1996; Giampiccolo et al., 2006). For seismic data, both approaches assume that Q_{sc}^{-1} is frequency-dependent while the Q_{in}^{-1} is frequency-independent. Seismic scattering attenuation is useful to invert for the scatterer sizes and the velocity deviation in the scatterers (Kang and McMechan, 1994). In GPR, separating Q_{in}^{-1} and Q_{sc}^{-1} and interpreting their origins has been done by Grimm et al. (2006), in which absorptions (Q_{in}^{-1}) are calculated from the DC resistivity and all remaining attenuation is attributed to scattering. They evaluate factors that control surface GPR signal penetration. However, separation of intrinsic (Q_{in}^{-1}) and scattering (Q_{sc}^{-1}) effects and estimating their parameters using GPR data alone have not previously been done; that is a goal we achieve in this paper.

Below, we describe a methodology to separate scattering and intrinsic Q^{-1} s in nonmagnetic media, extract the real conductivity and dielectric relaxation from the intrinsic attenuation, quantify scatterer sizes from GPR data, and apply it to one synthetic and three field crosshole data sets from an Ellenberger dolomite reservoir analog in central Texas. Then, we perform 2D interhole tomography for the real conductivity for the three crosshole data sets. Results of conductivity tomography and scattering are integrated with those from GPR crosshole velocity and surface data from Harbi and McMechan (2011).

METHODOLOGY

Solutions to Maxwell's equations in a low-loss medium can be reduced to the form of the wave equation for electromagnetic wave propagation (Annan, 1973; Keller 1987). For a 1D plane EM wave, the electric field is

$$E = E_0 \exp i(\omega t - kx). \quad (1)$$

In equation 1, the complex wavenumber (Turner and Siggins, 1994; Bradford, 2007; Giroux and Chouteau, 2010) is

$$k = \beta - i\alpha \quad (2)$$

where

$$\alpha = \omega \left[\frac{\mu\epsilon}{2} \left(\sqrt{1 + \left(\frac{\sigma}{\omega\epsilon} \right)^2} - 1 \right) \right]^{1/2}, \quad (3)$$

and

$$\beta = \omega \left[\frac{\mu\epsilon}{2} \left(\sqrt{1 + \left(\frac{\sigma}{\omega\epsilon} \right)^2} + 1 \right) \right]^{1/2}. \quad (4)$$

In equations 2–4, α and ω/β describe the attenuation coefficient and phase velocity v , respectively, where ω is the angular frequency; β is the phase factor; and σ , ϵ and μ are the complex, frequency-dependent electrical conductivity, dielectric permittivity, and magnetic permeability, respectively. The reciprocal of the quality factor Q is a dimensionless quantity that defines the energy loss per cycle, and is commonly used to describe attenuation (Aki and Richards, 1989). The total Q_t^{-1} is the composite of two additive components;

$$Q_t^{-1} = Q_{sc}^{-1} + Q_{in}^{-1}, \quad (5)$$

where Q_{in}^{-1} and Q_{sc}^{-1} are intrinsic and scattering Q^{-1} contributions, respectively (Dainty, 1981; Richards and Menke, 1983; Kang and McMechan, 1994; Grimm et al., 2006). Various methods for extraction of attenuation are based on amplitude spectra (Tonn, 1991), instantaneous frequency (Dasio et al., 2001), frequency shift (Quan and Harris, 1997), or spectral ratios (Báth, 1974). Below, we use the spectral ratio method because, unlike the other methods, the ratio is independent of the source spectrum (e.g., Behura and Tsvankin, 2009).

Intrinsic Q_{in}^{-1}

In GPR, the attenuation coefficient α is a combination of relaxation mechanisms of the frequency-dependent dielectric permittivity and magnetic permeability, and the real conductivity (equation 3) (Keller, 1987; Davis and Annan, 1989; Olhoeft and Capron, 1994; Xu and McMechan, 1997). Intrinsic Q_{in}^{-1} (the ratio of the conduction to the displacement currents [$\sigma/\omega\epsilon$] in equations 3 and 4) (Giroux and Chouteau, 2010), describes the attenuation of the electric field (Xu and McMechan, 1997). For nonmagnetic rocks, the magnetic permeability is the free space value (Olhoeft and Capron, 1994; Turner and Siggins, 1994). Then, the electric and dielectric parameters in equations 3 and 4 dominate the EM attenuation and velocity. They can then be grouped into the effective conductivity

$$\sigma_e = \sigma' + \omega\epsilon'', \quad (6)$$

and the effective permittivity

$$\epsilon_e = \epsilon' - \frac{\sigma''}{\omega}, \quad (7)$$

where ϵ' and ϵ'' are the real and imaginary dielectric permittivity, and σ' and σ'' are the real and imaginary electric conductivity (Turner and Siggins, 1994).

In the GPR frequency band, the imaginary electrical conductivity often is insignificant (Turner and Siggins, 1994; Xu and McMechan, 1997). So, in nonmagnetic rocks, the intrinsic attenuation is attributed to the combined effects of real conductivity σ' and

the relaxation of ϵ , described by ϵ'' . Setting $\sigma'' = 0$, the intrinsic attenuation (Q_{in}^{-1}) and the loss tangent [$\tan(\delta)$] of a GPR signal can be described (von Hippel, 1954; Keller, 1987; Turner and Siggins, 1994; Giroux and Chouteau, 2010) as

$$Q_{in}^{-1} = \tan(\delta) = \frac{\sigma_e}{\omega\epsilon_e} = \frac{\sigma'}{\omega\epsilon'} + \frac{\epsilon''}{\epsilon'}. \quad (8)$$

In low-conductivity media ($\tan \delta \ll 0.1$, which corresponds to $\sigma' < 1.0$ mS/m), the dielectric relaxation term ϵ''/ϵ' is dominant over $\sigma'/\omega\epsilon'$ (Turner and Siggins, 1994), and ϵ'' and ϵ' have very similar variations in frequency (Zhou et al., 2001). Therefore, Q_{in}^{-1} may be assumed to be constant over the GPR frequency range when σ is low (Turner and Siggins, 1994; Lui et al., 1998; Zhou et al., 2001; Bradford, 2007).

In the presence of conductivity, Q_{in}^{-1} is frequency-dependent (Daniels, 1996) because $\sigma'/\omega\epsilon'$ is a function of frequency. Figure 1 contains the intrinsic Q_{in}^{-1} (the thin solid line) calculated from the sum of the two Q_{in}^{-1} components in equation 8, from an arbitrary real conductivity of 5.0 mS/m (the dashed line) and a lab measurement of ϵ''/ϵ' (the dotted line) from an air-dried carbonate sample from an Ellenburger outcrop in central Texas. The components ϵ' and ϵ'' of the complex dielectric permittivity are measured with an HP-8752A network analyzer and an HP-8750A probe (Klein and Santamarina, 1997). For each sample, eight measurements are made at each of 101 frequencies between 20 MHz and 1.3 GHz (McMechan et al., 2002). In Figure 1, the decay rate of Q_{in}^{-1} with increasing frequency (the solid line) is defined by $\sigma'/\omega\epsilon'$ in frequency whereas ϵ''/ϵ' contributes only to the (nearly) constant Q_{in}^{-1} baseline at frequencies >40 MHz. Thus, for nonmagnetic rock, and for frequencies where ϵ'' and ϵ' vary similarly in frequency (Zhou et al., 2001) (>40 MHz for the Ellenburger lab data [Loucks et al., 1999]) and conductivity is real, Q_{in}^{-1} can be described by the sum of the ϵ''/ϵ' (frequency-independent) baseline and the (frequency-dependent) $\sigma'/\omega\epsilon'$. The upper limit of frequency independence is associated with the dielectric relaxation of water that occurs at frequencies above ~ 1 GHz. The following sections show synthetic and real data examples.

With increasing conductivity, EM velocity dispersion may occur (Keller, 1987). However, increasing ϵ' stabilizes the velocity for high conductivity (Reppert et al., 2000). For example, velocity is fairly constant for relative dielectric constants >5.0 for conductivity up to 20 mS/m for frequencies >40 MHz (Reppert et al., 2000), up to 100 mS/m in water (Davis and Annan, 1989). This is true for most geologic materials because increasing conductivity is commonly caused by the presence of ions dissolved in water, which also increases the relative dielectric constant; most geologic materials have dielectric constants 4–8, compared to 80 for water (Keller, 1987; Davis and Annan, 1989). In the presence of conductivity, and for a relatively large dielectric constant, the intrinsic Q_{in}^{-1} is a function of frequency, whereas the velocity dispersion is negligible (equations 3 and 4).

Scattering Q_{sc}^{-1}

Scattering attenuation is produced from the medium heterogeneity and is most efficient at wavelengths that are similar to the sizes of the scatterers in seismic and GPR propagation (Frankel and Clayton, 1986; Chang and McMechan, 1996; Hackert and Parra, 2003). Because of the strong similarities between GPR

and seismic wave behaviors (Fisher et al., 1992a, 1992b; Hollender et al., 1999; Lehmann et al., 2000; Bohidar and Hermance, 2002), most scattering models, empirical relationships, and applications proposed for acoustic and elastic waves, are also useful for EM waves.

For seismic waves, modeling of scattering and analytical and theoretical estimates of Q_{sc}^{-1} for different random media (Gaussian, exponential and self-similar) are discussed by Frankel and Clayton (1986), Frenje and Juhlin (2000), and Hackert and Parra (2003). Scattering attenuation calculated from the direct arrival signals is very similar to that calculated from signal codas (Frankel and Clayton, 1986). In self-similar models, with correlation distance A (the scatterer size), Q_{sc}^{-1} normally is distributed around peaks in the wavenumber (K), that correspond to the scatterer size; $KA = 1.0$ and $KA = 1.5$ for 2D and 3D media, respectively (Frankel and Clayton, 1986; Tang and Burns, 1992).

Total Q_t^{-1}

The total attenuation, Q_t^{-1} , as a composite of Q_{in}^{-1} and Q_{sc}^{-1} effects, can be estimated using various temporal or spatial forms, or in their respective Fourier transform domains (Aki and Richards, 1989). Methods for calculating Q_t^{-1} , and comparisons between them, are discussed by Jannsen et al. (1985), Tarif and Bourbie (1987), and Tonn (1989, 1991). The spectral ratio method (Báth, 1974; Jannsen et al., 1985; Aki and Richards, 1989; Rickett, 2007) is considered one of the best for Q measurement (Tonn, 1991). It measures the total Q as a function of frequency from the ratio of the amplitude spectra of the propagating waves transmitted between two spatially separated points using

$$\ln \left[\frac{A_1}{A_2} \right] = \ln \left[\frac{A_{01}}{A_{02}} \right] - \frac{\omega(x_2 - x_1)}{2vQ_t}, \quad (9)$$

where A_1 and A_2 are the spectral amplitudes of a GPR wave recorded at positions x_1 and x_2 , v is the phase velocity between x_1 and x_2 , and $[A_{01}/A_{02}]$ is a frequency-independent amplitude scaling that removes the source signature, geometrical spreading, and reflection and transmission losses (Jannsen et al., 1985; Neep et al., 1996; Rickett, 2007). In a crosshole GPR common-transmitter gather, A_{01}/A_{02} depends on the geometrical spreading as well as the source and receiver coupling and directivities (Zhou and Fullagar,

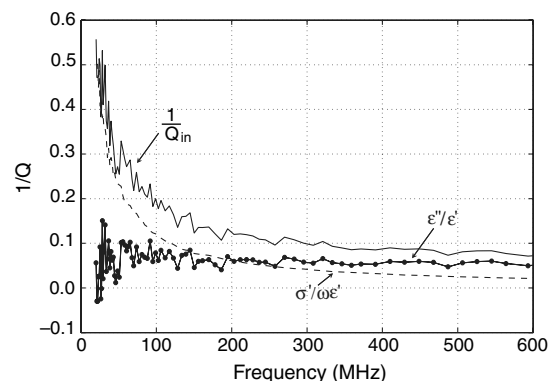


Figure 1. Calculated intrinsic total Q_{in}^{-1} (the thin solid line) for a representative conductivity of 5.0 mS/m (the dashed line), and for ϵ''/ϵ' (the dotted line) from lab measurements of a dolomite sample in the Ellenburger dolomite outcrop (Loucks et al., 1999).

2001), and equals 1.0 if both traces are corrected for the geometrical spreading and antenna directivity, and the source and receiver coupling are constant. Then, because $\ln(1) = 0$, equation 9 reduces to

$$\ln \left[\frac{A_1}{A_2} \right] = \frac{-\omega(x_2 - x_1)}{2vQ_t}, \quad (10)$$

and $Q_t^{-1}(\omega)$ becomes

$$Q_t^{-1}(\omega) = \frac{-2v \ln[A_1/A_2]}{\omega(x_2 - x_1)}. \quad (11)$$

For a known source wavefield, $Q_t^{-1}(\omega)$ is

$$Q_t^{-1}(\omega) = \frac{-2v \ln[A_r/A_s]}{\omega x}, \quad (12)$$

where A_s and A_r are the source and receiver amplitude spectral values, respectively, at radial frequency ω , and x is the distance along the raypath between the source and receiver.

Separation of Q_{in}^{-1} and Q_{sc}^{-1} and their parameter estimations

If the conductivity and relaxation components in Q_{in}^{-1} maintain their characteristic frequency behaviors, and if the velocity and transmitter-to-receiver raypaths are known (from velocity tomography), the real conductivity σ' and the dielectric relaxation ratio ϵ''/ϵ' between any crosshole source and receiver can be estimated by least-squares fitting of equation 8 to the calculated Q_t^{-1} . Figure 2 shows the total Q_t^{-1} (the open circles) calculated using spectral ratios from synthetic data for a 2D self-similar scattering model with correlation distance 1.0 m and homogenous conductivity (5.0 mS/m) and dielectric relaxation ϵ''/ϵ' ratio (0.10) backgrounds; the frequency range used is similar to that of the field data. The solid circles are the Q_t^{-1} for the same scattering model with zero conductivity and zero dielectric relaxation (only the scattering effect). Details of the modeling are discussed in the synthetic example section.

In Figure 2, Q_{in}^{-1} (the solid line) is the sum of the estimated ϵ''/ϵ' (the flat dashed line) and $\sigma'/\omega\epsilon'$ (the curved dashed line); ϵ''/ϵ'

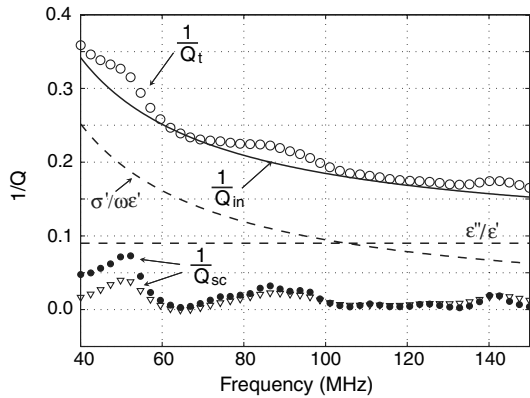


Figure 2. The open circles are the Q_t^{-1} calculated by the spectral ratio method. The solid line is the best least squares fit of intrinsic Q_{in}^{-1} to the total Q_t^{-1} . The dashed lines are the best estimates of the conductivity term $\sigma'/\omega\epsilon'$ and the dielectric relaxation term ϵ''/ϵ' (as labeled). The scattering contribution Q_{sc}^{-1} (the open triangles) is the difference between the total Q_t^{-1} and the estimated intrinsic Q_{in}^{-1} . The solid circles are Q_t^{-1} from the scattering model only (for $\sigma'/\omega\epsilon' = \epsilon''/\epsilon' = 0$).

gives the baseline, and $\sigma'/\omega\epsilon'$ gives the decay rate of Q_{in}^{-1} in frequency. The real permittivity ϵ' (equation 8) is calculated and updated from equation 4 for each σ' and ϵ''/ϵ' combination and the known phase velocity (from tomography), at the dominant frequency along the source-receiver raypath. Scattering Q_{sc}^{-1} is assumed to be an amplitude-reducing positive quantity in the total attenuation Q_t^{-1} of the propagating direct wave (equation 5) (Dainty, 1981; Richards and Menke, 1983; Kang and McMechan, 1994; Grimm et al., 2006). The estimated values σ' and ϵ''/ϵ' for this example are 5.3 mS/m and 0.09; the correct values are 5.0 mS/m and 0.10. The high estimated value of σ' is caused by the data truncation at 40 MHz, where there is still a significant influence of the scattering peak at ~ 52 MHz. This truncation, whose position is chosen to be consistent with the lowest reliable frequency in the field and lab data (Xu and McMechan, 1997; Rappert et al., 2000) (Figure 1) results, in this example, in a distortion of the best fit Q_{in}^{-1} curve to higher values and subsequent underestimation of the ϵ''/ϵ' and the Q_{sc}^{-1} values over the same frequencies. Compare the estimated Q_{sc}^{-1} curve (the triangles) with the correct Q_{sc}^{-1} curve (the filled dots) between 40 and 60 MHz.

Source estimation

The transmitter wavefield spectrum has to be known or estimated as a prerequisite of the total attenuation measurement in equation 12. So, here we introduce a procedure to approximate the transmitter wavefield spectrum. The Q_t^{-1} between any two crosshole receivers can be calculated using the spectral ratio (equation 11), but will not be reliable if the difference in the distances between the two receiver raypaths is too small (<3 wavelengths of the lowest frequency of interest) (Janssen et al., 1985; Frankel and Clayton, 1986). In GPR crosshole tomography surveys, the receiver depth increment is usually less than a wavelength (see the acquisition parameters for the field data, below).

To estimate the source wavefield spectrum, we assume the transmitter and receiver coupling in the holes is constant across a single common-transmitter gather. Then, we perform four steps: First, we estimate Q_t^{-1} as a function of frequency from the spectral ratio between all receiver pairs in the same common-transmitter gather, whose raypath lengths differ by more than three wavelengths (Janssen et al., 1985) (equation 11). This includes sources and receivers at large angles from horizontal. The second step is to estimate the Q_{in}^{-1} as a function of frequency by fitting $\sigma_e/\omega\epsilon_e$ from equation 8 to Q_t^{-1} as described in the previous subsection. This is repeated for all common-transmitter gathers between a pair of holes, which are then averaged to minimize any scattering contribution in the Q_{in}^{-1} approximation in each interhole area.

The third step is to find, in each common-transmitter gather, those receiver spectra (A_r) that have smooth variations (no spikes or interference patterns), which indicates low scattering effects. Then, these are used to estimate the source amplitude and centroid frequency by back-calculating from the amplitude A_r at each receiver and each frequency ω , with the approximate Q_{in}^{-1} between holes, using

$$\langle A_{es} \rangle = \left\langle \frac{x}{\cos \theta_s \cos \theta_r} A_r \exp\left(\frac{\omega x}{2vQ_{in}}\right) \right\rangle, \quad (13)$$

where $x/[\cos(\theta_s)\cos(\theta_r)]$ compensates for geometrical spreading for ray length x and antenna directivity at ray angle θ_s at the source.

This is an adaptation of the seismic attenuation tomography by Brzostowski and McMechan (1992). The estimated average source spectrum over all the receivers, at radial frequency ω , is $\langle A_{es} \rangle$, and v is the velocity; x , θ_s , and θ_r are calculated a priori by ray tracing in the velocity model obtained by interhole velocity tomography (Zhou and Fullagar, 2001; Harbi and McMechan, 2011).

Calibration traces recorded in air preserve the source wavefield spectrum shape as there is no scattering and no attenuation of EM waves in air. In the current crosshole tomography data acquisition, calibration traces are recorded at a known distance in air for estimation of the transmitter excitation time (Harbi and McMechan, 2011). These traces also are used to estimate the source spectrum because amplitude spectra at receivers in the crosshole survey are modified from the source spectrum by the attenuation (Quan and Harris, 1997). Thus, in the fourth step, we estimate the source spectral shape (A_s in equation 12 for each source position from the calibration trace spectrum, and its dominant amplitude and frequency are calibrated from the maximum amplitude of $\langle A_{es} \rangle$ in the third step.

SYNTHETIC EXAMPLE

Finite-difference solution of Maxwell's equations is a good choice for synthesizing GPR intrinsic and scattered waves. We use the Xu and McMechan (1997) code that solves Maxwell's equations by finite-differencing in the time and space domain; it simulates intrinsic attenuation with dielectric and magnetic relaxations, and the real conductivity with the Debye equation using the Cole-Cole formulation (Cole and Cole, 1941; Debye, 1945).

For nonmagnetic rock, the input parameters used for generating synthetic GPR data are in Table 1; these are Cole-Cole (Cole and Cole, 1941) parameters of carbonate samples, calculated by Taherian et al. (1990). Figure 3a shows a 2D self-similar scattering model for a 1.0 m correlation distance. This model is created by filtering a 2D (horizontal \times vertical) = (56 \times 60) cell model grid with an 0.25 m increment in both directions, populated with the properties of the ten (normally distributed) materials in Table 1. The filtering is done by 2D Fourier transforming the model, then multiplying the two axes of the 2D wavenumber spectrum of the model by $A/(1 + A^2K^2)^{-1/2}$, where K is the wavenumber and A is the correlation distance (the scatterer size) and then transforming back to space (Frankel and Clayton, 1986; Kang and McMechan, 1994). For such a model, the grid increment has to be less than the correlation distance A and the physical model size has to be $>2\pi A$ (Frenje and Juhlin, 2000). For reference, the corresponding conductivity distribution is in Figure 3b.

Synthetic GPR data for this scattering model are simulated using a 100 MHz infinitesimal dipole with a Ricker source in time, that is in the 2D plane, at 8.0 m depth (in hole H1 in Figure 3a); the vertical component of the electric field (Figure 3c) is saved at receiver points (in hole H2) with 0.25 m increments. Synthetic data also are generated for the same scatterer distribution for three different constant conductivities (1, 5, and 10 mS/m) and for four different constant permittivity relaxation ratios (0.01, 0.05, 0.10, and 0.30) as backgrounds. These models are used to test the reliability of the proposed methodology

and its ability to separate and estimate the scattering and intrinsic attenuation parameters for different conductivities and relaxations.

To test the proposed methodology with 2D synthetic data, we first correct the data for the source and receiver directivities using the homogenous dipole directivity approximation ($\cos \theta_s \cos \theta_r$) (Holiger et al., 2001; Zhou and Fullagar, 2001), and for the infinitesimal dipole geometrical spreading ($1/\sqrt{r}$) (Hamstad et al., 2001), where θ_s and θ_r are the propagation angles (from horizontal) at the source and receiver points, respectively, and r is the distance along the propagation path from the source to the receiver. Then, we apply a tapered 30 ns time window around the direct arrival waves to minimize coda contributions in the attenuation calculations, and Fourier transform the data traces over time to get the receiver spectra. Next, we calculate the total Q_T^{-1} as a function of frequency from equation 12 using an estimated source wavefield spectrum as described in the previous section. Finally, we estimate and separate each of the Q_T^{-1} components using the procedure described above.

For the scattering model (Table 1, Figure 3a) and the recording geometry in Figure 3a, Figure 4a shows the average Q_T^{-1} (the open circles) and the average of the best least-squares fits (the solid line) to the Q_T^{-1} for all receiver pairs with greater than three wavelengths difference between their raypath lengths. Figure 4b shows the estimated amplitude spectrum of the source wavefield (the solid line) using the shape of the frequency spectrum of a common-depth trace in a nonattenuating model (not shown) and the average amplitude spectrum obtained by back-calculating the spectra for those receivers with low scattering in the common-transmitter gather (the dashed line), which is compared to the actual source spectrum used in the model (the dotted line). The velocity used, for the source and Q_T^{-1} , Q_{in}^{-1} , and Q_{sc}^{-1} estimation and separation, is obtained from the first arrival time and the source-receiver paths traced in a smoothed version of the scattering model (Figure 3a). Smoothing is required because of the limitations of ray tracing in scattering models (Crossley and Jensen, 1989; Williamson, 1991).

Figure 5 contains the total, intrinsic, and scattering Q^{-1} versus frequency, estimated for the common-depth trace (at the star at 8.0 m depth in the synthetic data in Figure 3b) for three models, each with a different homogenous conductivity background and

Table 1. Cole-Cole parameters for water-saturated carbonate rocks (Taherian et al., 1990); relative dielectric constant values at low and high frequency (ϵ_o and ϵ_∞), respectively; relaxation exponent factor (α); relaxation time τ ; real conductivity (σ).

Material	ϵ_o	ϵ_∞	α	τ (ns)	σ (mS/m)
(1)	12.02	8.65	0.231	8.4	5.09
(2)	17.24	10.84	0.261	17.1	2.33
(3)	19.25	11.86	0.258	25.1	4.39
(4)	20.12	10.37	0.246	11.3	3.60
(5)	22.65	9.83	0.407	133.4	1.37
(6)	29.49	11.62	0.340	29.5	7.32
(7)	33.33	13.95	0.228	16.2	11.24
(8)	35.05	9.35	0.466	768.8	1.56
(9)	35.70	14.59	0.240	22.8	9.67
(10)	46.64	20.53	0.131	12.0	9.0

the same relaxation model ($\epsilon''/\epsilon' = 0.10$), which are a subset of the tests described above. The intrinsic Q_{in}^{-1} (dashed) lines are strong functions of frequency for the high conductivity values (5.0 and 10.0 mS/m) and nearly flat, and close to the ϵ''/ϵ' value for the 1.0 mS/m conductivity. Tables 2 and 3 show the input and estimated values for each of the constant conductivity and relaxation combinations in the models.

The frequency axis (at the bottom) of Figure 5 is converted into $1/\text{wavenumber}$ (at the top) using the average velocity over all transmitter-receiver raypaths to give an approximate scale of scatterer size ($KA = 1$ for 2D); the dominant scatterer size

corresponds to the peaks in the scattering spectrum. In Figure 5, the estimated dominant scatterer size is ~ 0.9 m compared to the 1.0 m correlation length in the model. There is a range of scattering over K^{-1} from ~ 0.65 to ~ 1.15 m, which includes the correct value (each trace produces a different estimate).

Having shown above that, for a homogenous background of σ' and ϵ''/ϵ' , their parameters are accurately recovered, we now consider estimation of the full heterogeneous model (Table 1 and Figure 3a). For the heterogeneous conductivity distribution, the estimated and actual conductivities (the solid and dashed lines, respectively) for each trace in Figure 3c are plotted versus receiver depth in Figure 3d. The estimated conductivity is calculated using the proposed methodology using transmitter-to-receiver raypaths traced in a smoothed version of the scattering model. For the comparison in Figure 3d, the correct conductivity values are those in the original scattering model in Figure 3b, along the rays in the smoothed model. Only the average ϵ''/ϵ' , which equals ~ 0.02 , is estimated for the model.

FIELD DATA EXAMPLE

The Ellenburger is a Lower Ordovician shallow-water carbonate that is ~ 520 m thick in west Texas, where it is a reservoir (Kerans, 1988; Loucks et al., 1999; McMechan et al., 2002). The reservoir porosity and permeability are associated with secondary dolomitization (Amthor and Friedman, 1991), and karsting dissolution and fractures that are attributed to the tectonics and the collapsed paleocave history (Loucks et al., 1999; Loucks et al., 2004; Gale and Gomez, 2007). The study volume contains disturbed host rocks (facies 3) and coarse- and fine-clast chaotic breccia facies (facies 4 and 5) that developed through three periods of alternating surface exposure and burial, from Middle Ordovician to the present (Loucks and Anderson, 1985; Kerans, 1988; Loucks et al., 1999; Gale and Gomez, 2007). Orientation and distributions of the porosity and permeability in the Ellenburger reservoir are controlled by the density and orientation of the conjugate fracture system (McMechan et al., 2002; Harbi and McMechan, 2011). Two set of fractures are identified (Gale and Gomez, 2007) in well cores from west Texas, and through 2D and 3D GPR reservoir analog characterization in the reservoir outcrop in central Texas (McMechan et al., 2002; Harbi and McMechan, 2011). These fractures are a northwest-southeast and northeast-southwest conjugate set associated with the Pennsylvanian Ouachita orogeny, and an irregular orientation and distribution associated with the collapsed paleocave systems (Gale and Gomez, 2007; Harbi and McMechan, 2011). The geologic context, and petrophysical and electrical property measurements from core samples can be found in Loucks et al. (1999, 2004), McMechan et al. (2002), and

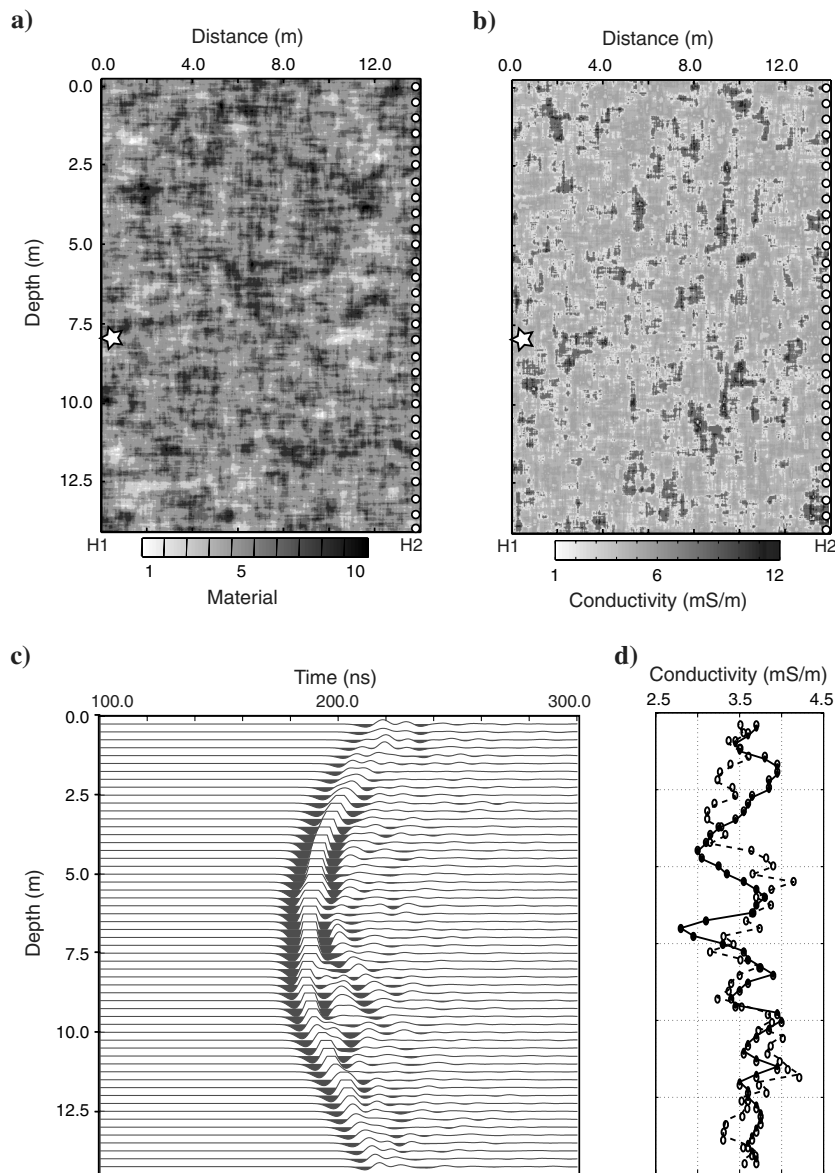


Figure 3. (a) A self-similar model with correlation distance = 1.0 m; material refers to the 10 sets of electric and dielectric parameters in Table 1. (c) Contains the synthetic crosshole GPR data for a dipole source at 8.0 m depth in hole H1, and receivers every 0.25 m depth in hole H2. (d) The correct (dashed line) and estimated (solid line) average conductivity between the source and receivers for the data in (c). In (a) and (b), the star is the source location; the white dots are the receivers. For reference, (b) is the the conductivity distribution corresponding to the material properties in (a).

Koesoemadinata and McMechan (2003). Some of the data from these previous studies are used below, for comparison.

The following example uses three field crosshole tomography data sets from an Ellenburger dolomite outcrop in central Texas (Figure 6) (Harbi and McMechan, 2011). These consist of GPR crosshole tomography data between three pairs of holes and a 3D surface data volume on a grid surrounding the three holes. Only the crosshole GPR data are used in this paper for attenuation analysis. The GPR crosshole data are acquired using a PulseEKKO IV GPR system with 100 MHz nominal frequency borehole antennas. The transmitter voltage is 1000 V and 128 traces are stacked to form each recorded trace.

The tomography survey involves fixing the transmitter antenna in one borehole while the receiver antenna is moved in 0.25 m depth steps to the maximum depth of the holes (15.0 m); this is then repeated for each 0.25 transmitter step (Figure 7a). The starting depth for both antennas is 1.25 m to minimize the signal complexity at the earth/air interface (Hammon III et al., 2002; Holliger and Bergmann, 2002). The data include calibration traces recorded in the air between two points of known separation; these are used for calculating the transmitter excitation time (Harbi and

McMechan, 2011) and the transmitter spectrum (Figure 4). Figure 7b shows a representative crosshole GPR scan for a transmitter at 8.0 m depth in hole UT1 and receivers in hole C10.

The surface 3D GPR data, which provide the structural context and porosity and permeability estimations (Harbi and McMechan, 2011) are acquired using a PulseEKKO IV GPR system with antennas of 50 MHz nominal frequency. The survey is along 35 north–south profiles of 25 m length and 0.5 m separation using a constant offset of 3 m and 0.25 m station separation. Details

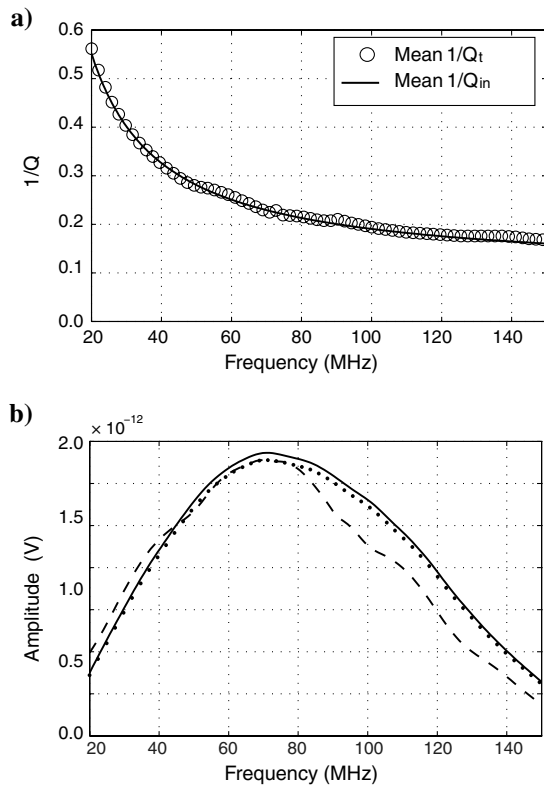


Figure 4. Average of the total Q_t^{-1} (the open circles) and the average of the best fit intrinsic Q_t^{-1} (the solid line) for all receiver pairs with separation more than three wavelengths. $\sigma' = 10.0$ mS/m and $\epsilon''/\epsilon' = 0.10$ for the single source at 8.0 m depth in the synthetic scattering model in Figure 3a. (b) The estimated source wavefield spectrum (the solid thin line) from the magnitude of A_{es} [the dashed line in (b), equation 13] obtained using Q_{in}^{-1} in (a) and the shape of receiver spectrum in the nonattenuating and nonscattering model; the dotted line in (b) is the actual source wavefield spectrum of a 100 MHz Ricker source for the same model as in (a). In (a) only every fourth data point is plotted, for clarity.

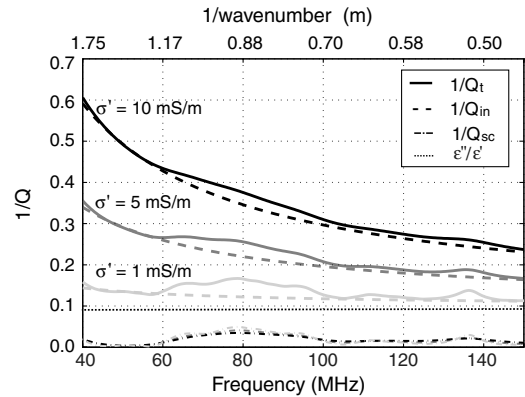


Figure 5. Calculated total, intrinsic, and scattering Q^{-1} for the single common depth trace at 8 m depth for synthetic GPR data in the scattering model in Figure 3a, for homogenous conductivity backgrounds of 1, 5 and 10 mS/m, and constant $\epsilon''/\epsilon' = 0.10$; the observed intrinsic Q_{in}^{-1} is the sum of the estimated conductivity response $\sigma'/\omega\epsilon'$ and the estimated dielectric relaxation ϵ''/ϵ' . The dotted line is the mean of ϵ''/ϵ' estimations for the three conductivity values.

Table 2. Input and estimated σ' for different homogeneous ϵ''/ϵ' backgrounds in the scattering model in Figure 3a. Values between parentheses are the relative estimated error in percent.

Input σ' (mS/m)	0.010	Input 0.050	(ϵ''/ϵ') 0.100	0.300
1.00	0.75 (25)	0.76 (24)	0.76 (24)	0.50 (50)
5.00	5.10 (2)	5.20 (4)	5.20 (4)	5.20 (4)
10.00	10.90 (9)	10.90 (9)	11.10 (11)	10.80 (8)

Table 3. Input and estimated ϵ''/ϵ' for different homogenous σ' backgrounds in the scattering model in Figure 3a. Values between parentheses are the relative estimated error in percent.

Input σ' (mS/m)	0.010	Input 0.050	(ϵ''/ϵ') 0.100	0.300
1.00	0.009 (10.00)	0.049 (2.00)	0.099 (1.00)	0.299 (0.33)
5.00	0.009 (10.00)	0.049 (2.00)	0.099 (1.00)	0.299 (0.33)
10.00	0.012 (20.00)	0.052 (4.00)	0.103 (3.00)	0.303 (0.01)

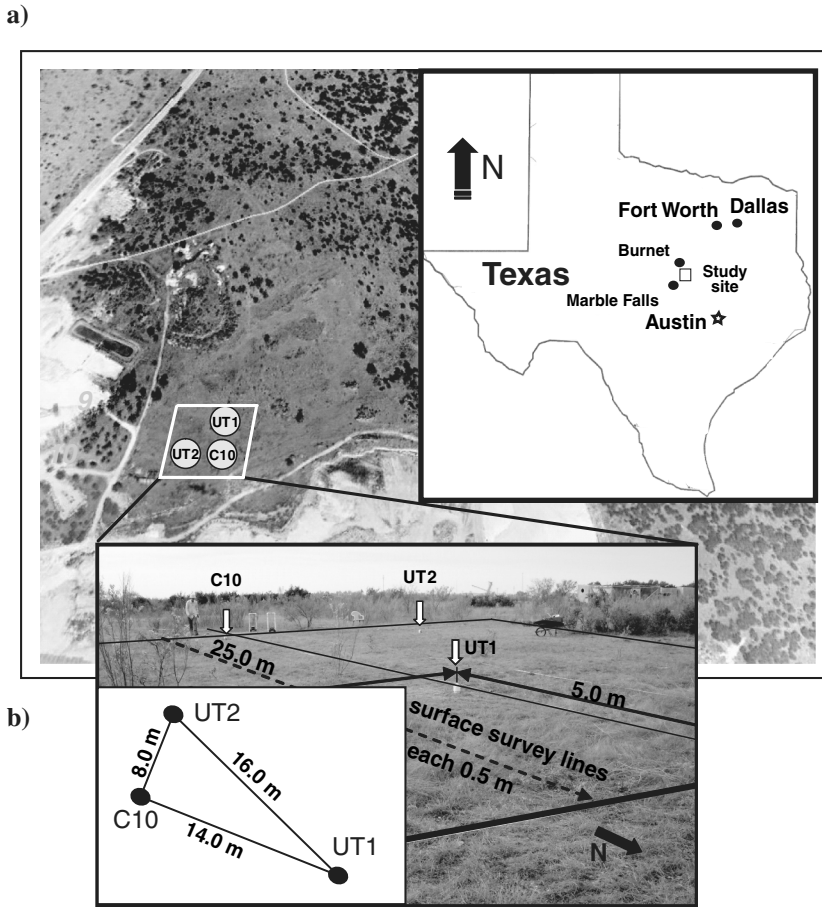


Figure 6. (a) Aerial photo of the survey site in Marble Falls area, central Texas (north-west of Austin). (b) The hole locations and the surface survey lines; the relative hole locations are in the inset in (b) (modified from Harbi and McMechan (2011)).

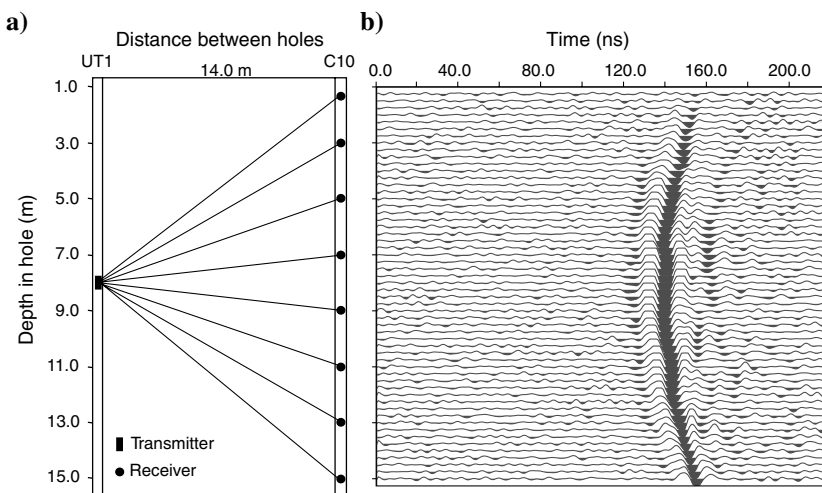


Figure 7. (a) A single common-transmitter gather survey geometry for crosshole tomography between holes C10 and UT1; the tomography survey consists of 0.25 m transmitter and receiver depth increments in both holes. (b) is a representative crosshole common-transmitter gather scan for the transmitter at 8.0 m depth in hole UT1; in (a) receivers are plotted at 2.0 m interval for clarity.

of the data acquisition and processing are in Harbi and McMechan (2011).

Estimation of the Q_{in}^{-1} conductivity and dielectric relaxation components, and the Q_{sc}^{-1} contributions to the total attenuation Q_t^{-1} in the field data are done as illustrated above in the synthetic examples, except for the following changes. We use $1/r$ instead of $1/\sqrt{r}$ to correct for the 3D geometrical far-field spreading because the data are acquired with center-fed dipole antennas in 3D (Sato and Thierbach, 1991; Zhou and Fullagar, 2001; Irving, 2006), where r is the distance between the source and receiver calculated along a curved raypath in the velocity model between the holes (Harbi and McMechan, 2011). The approximate antenna directivity term $\cos \theta_s \cos \theta_r$ is used for the crosshole survey between the 10-cm-diameter air-filled holes (Holliger et al., 2001; Zhou and Fullagar, 2001). The angles θ (measured from horizontal) are extracted for each transmitter-receiver ray, from the ray tracing in the velocity model. A 40 ns time window around the direct arrival waves is sufficient to include the complete direct arrival wavelets for applying the FFT and to minimize coda contributions. The source wavefield strength (A_s in equation 12) is estimated for each source position separately as described above. Finally, the scatterer size is $\sim 1.5/\text{wavenumber}$ for 3D propagation (Tang and Burns, 1992).

Figure 8a and 8b shows the estimated σ' and ϵ''/ϵ' , respectively, versus the average angle (from horizontal) between transmitter and receivers, between the hole pair C10 and UT1. Conductivity is anisotropic (Figure 8a); the conductivity is higher as the angle from horizontal increases. This is expected because the velocity in this area also is anisotropic (Harbi and McMechan, 2011), and velocity and conductivity vary inversely (equation 4). The two components in the dielectric relaxation (ϵ' and ϵ'' , Figure 8b) also are anisotropic, but because both have the same anisotropy, the anisotropy cancels when the ϵ''/ϵ' ratio is taken. In equation 8, σ' and ϵ'' play similar roles; attenuation increases as either increases.

The ϵ''/ϵ' values estimated from the GPR data between the hole pair C10 and UT1 (Figure 8b) fluctuate around a mean value of 0.024 ± 0.023 compared to the mean of $\sim 0.05 \pm 0.009$ from 15 lab measurements from core samples with ambient saturation from hole C10; these 15 core measurements are spaced at 1.0 m depth intervals (Loucks et al., 1999). The ϵ''/ϵ' ratios estimated from the GPR data are small and have large standard deviations. Some of the values in Figure 8b are negative, which is unphysical, and is a consequence of the $\sigma'/\omega\epsilon'$ fit being too low in Q_{in}^{-1} . The latter

reflects the assumptions and accumulated uncertainties in the prior steps, specifically the assumptions of a homogeneous average σ' and constant receiver coupling, and the subjective nature of defining the traces with low scattering when estimating the source strength. The accumulated consequence of all of these is an underestimation of source strength, which is consistent with, and is the most likely cause of, the negative values in Figure 8b. If the ϵ''/ϵ' values all are shifted up by one standard deviation, to make most of the values positive, the mean ratio becomes nearly the same as that from the core measurements; this would also involve shifting the $\sigma'/\omega\epsilon'$ values upward to larger Q_{in}^{-1} by the same amount. Because of their sampling, the core measurements are not necessarily more representative than those from the GPR data, so they serve mainly to confirm the approximate order of magnitude. In view of this uncertainty, only the $\sigma'/\omega\epsilon'$ and scattering contributions are estimated for the other two pairs of holes.

Figure 9a is a representative example of the total, intrinsic, and scattering components of Q^{-1} for the field data trace for the transmitter at 8.0 m depth in hole UT1 and the receiver at 1.5 m depth in hole C10. The scattering spectra in the total Q^{-1} for all receivers in hole C10 from the common-transmitter gather in Figure 7b are plotted versus depth in Figure 9b. The horizontal ($1.5/K$) axis in Figure 9b shows the 3D scatterer size distribution, obtained using the average velocity along the corresponding raypaths.

Scattering attenuation spectra for the common (transmitter and receiver) depth data for all three pairs of holes (UT1-C10, UT2-C10, and UT1-UT2) are plotted in Figure 10a, 10b, and 10c, versus depth and scatterer size. In Figures 10 and 9b, larger scatterer sizes

are seen near the top and bottom of the models, and smaller in between, which are consistent with the known facies distribution (Harbi and McMechan, 2011). The average breccia sizes are <0.30 from ~ 7.0 to ~ 13.0 m depth, and predominantly ~ 0.3 m to ~ 0.45 m outside this depth range. In Figure 10b, the dominant scatterer size and range are smaller than in 10b and 10c because UT2-C10 is approximately perpendicular to the dominant regional (Ouachita) fracture system (Gale and Gomez, 2007); larger breccia sizes are expected in the direction parallel to fractures rather than perpendicular to them. Similarly, the higher magnitudes of scattering in Figure 10b also are consistent with this line orientation; the fracture density observed by Gale and Gomez (2007) is $1.8 - 4.0 \times 10^4$ fractures/m², for fractures above 1 mm wide. Most of these are near vertical and so are not apparent as individual features in the surface GPR data, although they contribute to the scattering perpendicular to them.

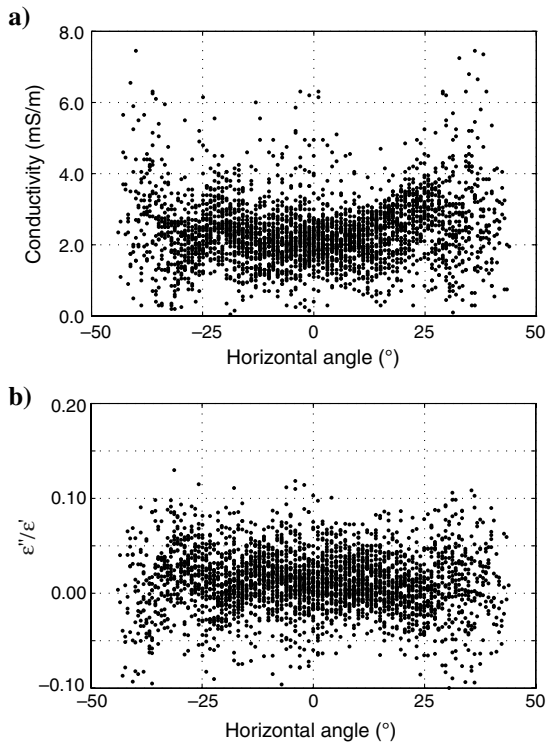


Figure 8. Estimated (a) real conductivity σ' and (b) ϵ''/ϵ' for all crosshole data between holes C10 and UT1, versus angle between transmitters and receivers from horizontal; positive angles correspond to a transmitter deeper than a receiver.

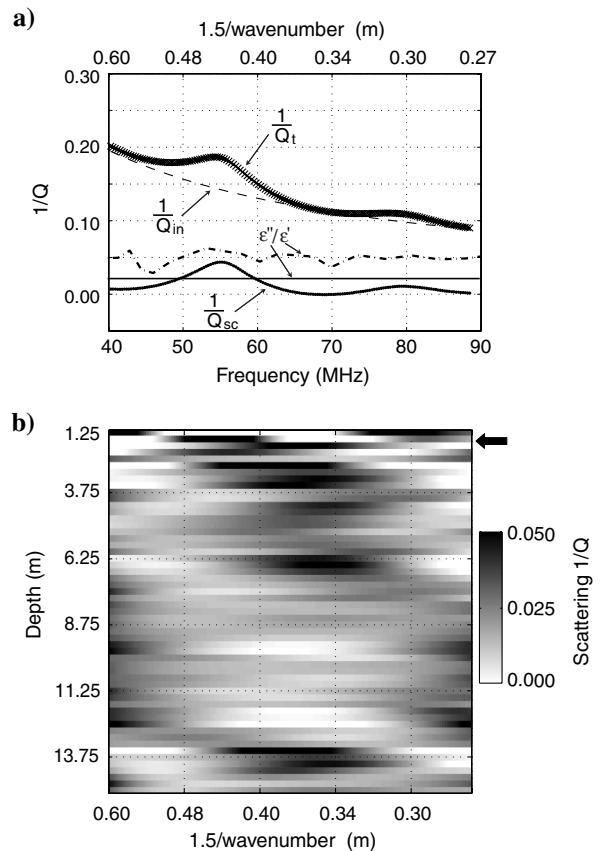


Figure 9. (a) Calculated total, intrinsic, and scattering Q^{-1} , and dielectric relaxation for a single representative source at 8.0 m depth in UT1 and a receiver at 1.5 m depth in hole C10 (from the common-transmitter gather in Figure 7b); the solid horizontal and dot/dash lines are the estimated ϵ''/ϵ' , and the average measured from 15 core samples in hole C10, respectively. (b) Scatterer size spectra extracted from the total Q^{-1} for all traces in the common-transmitter gather shown in Figure 7b. The black arrow in (b) indicates the location of receiver for the trace in the example in (a); the amplitudes in this slice are the same as those in the Q_{sc}^{-1} curve in (a). The $1.5/\text{wavenumber}$ scale in (a) and (b) is calculated from the frequencies and the average velocity along the corresponding source-to-receiver raypath, to give approximate scatterer sizes.

2D CONDUCTIVITY TOMOGRAPHY

The intrinsic attenuation coefficient α (nepers/m) and the real conductivity σ' are heterogeneously distributed intrinsic medium parameters that can be represented by homogenous values of apparent attenuation α_a and apparent real conductivity σ'_a over a raypath (Won, 2011). The effective attenuation α_e denotes the composite intrinsic attenuation effect of σ' and ϵ''/ϵ' , along the raypath (Rickett, 2007).

From equations 1 and 2, the electrical field amplitude for a 1D plane wave is given by

$$E = E_0 e^{i(\omega t - \beta x)} e^{-\alpha_e x}, \quad (14)$$

where α_e is the effective attenuation (in nepers) on the path of length x (Zhou and Fullagar, 2001; Rickett, 2007) and is related to the apparent attenuation α_a (nepers/m) (Zhou and Fullagar, 2001) through

$$\alpha_e = \alpha_a x. \quad (15)$$

In seismic and GPR wave propagation, the effective attenuation is the line integral of the attenuation distribution α (nepers/m) along the raypath (Brzostowski and McMechan, 1992; Dobroka et al., 1992; Zhou and Fullagar, 2001; Rickett, 2007)

$$\alpha_{e_k} = \int \alpha_j dl_j, \quad (16)$$

where α_{e_k} is the observed effective attenuation coefficient along ray k , α_j is the attenuation (in nepers/m) of the cell that segment j crosses, and dl_j is the length of segment j .

In GPR, the attenuation coefficient α_j is related to the loss tangent [$\tan(\delta_j)$] for any segment j of the raypath as (Turner and Siggins, 1994)

$$\alpha_j = \frac{\omega \tan(\delta_j)}{2v_j} = \frac{\sigma'_j}{2v_j \epsilon'_j} + \frac{\omega}{2v_j} \left(\frac{\epsilon''_j}{\epsilon'_j} \right). \quad (17)$$

Then, from equations 15 and 17, equation 16 can be reformed into

$$\begin{aligned} \alpha_{e_k} &= \frac{x\sigma'_a}{2v_a \epsilon'_a} + \frac{x\omega}{2v_a} \left(\frac{\epsilon''_a}{\epsilon'_a} \right) \\ &= \int \frac{1}{2v_j \epsilon'_j} \sigma'_j dl_j + \int \frac{\omega}{2v_j} \left(\frac{\epsilon''_j}{\epsilon'_j} \right) dl_j, \end{aligned} \quad (18)$$

where v_j and σ'_j are the velocity and the real conductivity of the cell that segment j crosses, and ϵ'_j and ϵ''_j are the real and imaginary

dielectric permittivity in segment j along the raypath k , respectively. For a nondispersive, low conductivity, and nonmagnetic medium, as we have in the current study, ϵ' can be approximated by $v = \sqrt{1/\mu_0 \epsilon'}$ (Davis and Annan, 1989; Cai and McMechan, 1995; Annan, 1996; Zhou and Fullagar, 2001). Errors in estimating ϵ' using the low-loss approximation in a lossy medium at 100 MHz dominant frequency are <6.0% for conductivity of 30.0 mS/m and dielectric constant of 11.0 (Giroux and Chouteau, 2010). Thus, omitting the terms containing ϵ''_j/ϵ'_j in equation 18 and writing the rest in discrete form gives

$$xv_a \sigma'_a = \sum_{j=1}^m v_j \sigma'_j dl_j, \quad (19)$$

where v_j is provided by the velocity tomography; x is the total ray-path length calculated by ray tracing in velocity model v_j ; v_a is the average (apparent) velocity along the raypath calculated from the traveltimes and the raypath distance x ; σ'_a is calculated from the fitting to Q_{in}^{-1} as described above; m is the number of ray segments; and dl_j is the length of ray segment j (see Brzostowski and McMechan [1992] for the seismic equivalent).

Equation 19 is a linear relation between the observed apparent velocity and real conductivity (v_a and σ'_a), and the local velocity and conductivity values (v_j and σ'_j , respectively, in each cell that the ray crosses), which can be solved as a linear inverse problem

$$\mathbf{A} = \mathbf{D}\mathbf{s}^T, \quad (20)$$

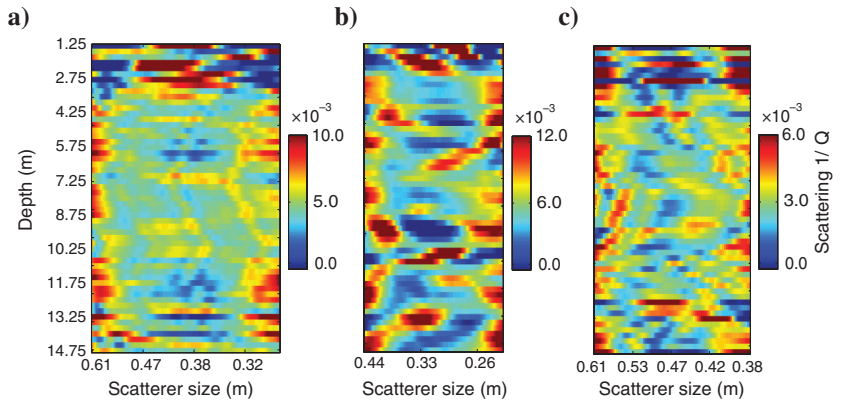
where \mathbf{s} is an $mn \times 1$ vector of the real conductivity distribution, which we solve for, as

$$\mathbf{s} = [\sigma'_{11} \quad \sigma'_{12} \quad \dots \quad \sigma'_{1n} \quad \sigma'_{21} \quad \sigma'_{22} \quad \dots \quad \sigma'_{2n} \quad \dots \quad \sigma'_{mn}], \quad (21)$$

\mathbf{A} is the $(m \times 1)$ observation vector for apparent velocity and real conductivity as

$$\mathbf{A} = \begin{bmatrix} x_1 v_a \sigma'_a \\ x_2 v_a \sigma'_a \\ \vdots \\ x_m v_a \sigma'_a \end{bmatrix}, \quad (22)$$

Figure 10. Scatterer size spectra versus depth for common transmitter and receiver depths between holes (a) UT1-C10 (b) UT2-C10, and (c) UT1-UT2. Scatterer size scales are calculated as 1.5/wavenumber; note that the scatterer and dominant size scales increase from right to left.



and \mathbf{D} is the $m \times mn$ array containing velocity and segment lengths of each observation in the $(m \times n)$ model obtained from a priori velocity tomography as

$$\mathbf{D} = \begin{bmatrix} v_{11}d_{11} & v_{12}d_{12} & \dots & v_{1n}d_{1n} & v_{21}d_{21} & v_{22}d_{22} & \dots & v_{2n}d_{2n} & \dots & v_{mn}d_{mn} \\ v_{11}d_{11} & v_{12}d_{12} & \dots & v_{1n}d_{1n} & v_{21}d_{21} & v_{22}d_{22} & \dots & v_{2n}d_{2n} & \dots & v_{mn}d_{mn} \\ \vdots & \vdots \\ v_{11}d_{11} & v_{12}d_{12} & \dots & v_{1n}d_{1n} & v_{21}d_{21} & v_{22}d_{22} & \dots & v_{2n}d_{2n} & \dots & v_{mn}d_{mn} \end{bmatrix} \quad (23)$$

Each row in \mathbf{D} contains mostly zeros except for those cells that a particular observation ray passes through (McMechan et al., 1987). We use the simultaneous iterative reconstruction technique (SIRT) (Dines and Lytle, 1979; McMechan et al., 1987; Zhu and McMechan, 1989; Brzostowski and McMechan, 1992; Dobroka et al., 1992) to solve equation 20 for \mathbf{s} using the known velocity and ray distributions in \mathbf{D} , which also is solved (a priori) using SIRT by Harbi and McMechan (2011).

Velocity tomography is a prerequisite to conductivity tomography; velocity tomography provides the velocity distribution and the raypaths. In velocity tomography, SIRT traces rays using two-point ray tracing (Um and Thurber, 1987) and perturbs the raypaths to satisfy Fermat's principle of minimum time. Then, SIRT uses the time residual between the observed and calculated times to update the velocity model until a stable minimum time residual is achieved (Zhu and McMechan, 1989; Brzostowski and McMechan, 1992).

In conductivity tomography, raypaths are input and only the real conductivity model is iteratively updated using different anisotropy ratios to minimize the residual between the observed and calculated apparent conductivity σ'_a . Initial horizontal real conductivity models for each pair of holes in the real conductivity tomography are calculated from the observed apparent conductivity from the common-depth traces between holes. For tomography between each pair of holes, the model is discretized into a 0.25×0.25 m grid of square cells. The anisotropy of the conductivity (the ratio of the vertical/horizontal conductivity) is included as described by Hammon III et al. (2002) for calculating the VTI velocity anisotropy. The local orientation angle of the ray-segment within each cell is used to calculate the conductivity deviation from the horizontal component for every cell along the raypath in the model. A series of solutions is performed, each for a different anisotropy value, searching for the one that gives the best fit to the observed attenuation data, which is accepted as the solution.

For each anisotropy value, 150 iterations are performed, after which the model is despiked and smoothed using a 2D moving average and median filter of 5 grid points extending in vertical and horizontal directions (Arias-Castro and Donoho, 2009) before doing another set of iterations, until steady minimum residuals are achieved. This regularization of the solution eliminates discontinuities caused by cells that are not sampled and stabilizes the solution when noise is present (Dines and Lytle, 1979).

Figure 11a shows the calculated versus observed apparent real conductivity (σ'_a) for all raypaths between the C10-UT1 hole pair, which give the correlation coefficient $R^2 = 0.922$. The other two hole pairs have similar outputs, with correlation coefficients ($R^2 = 0.901$ and 0.928 for holes C10-UT2 and UT1-UT2, respectively). The best real conductivity anisotropy is found to be with the vertical/horizontal real conductivity ratio (σ'_v/σ'_h) = 1.07 over all

three pairs of holes; this ratio is the reciprocal of that found for the velocity (0.93) by Harbi and McMechan (2011), so it is internally consistent. Figure 11b shows the (observed — calculated) residual of the real conductivity as a function of propagation angle; most of these data lie near the zero residual line, indicating that the estimated anisotropy is accurate. The farthest outliers are possibly caused by unreliable measurements in low S/N regions (as they correspond to the longest propagation paths), but more likely by multipathing with a low-conductivity path segment critically refracting along an air-filled borehole. The model contains three different facies that can be separated using the GPR attributes (Harbi and McMechan, 2011). Each facies may present a different velocity and real conductivity anisotropy ratio (Harbi and McMechan, 2011), but the limitation of the tomography inversion, and lack of additional information to quantify these, restricts us to accept an average anisotropy ratio for the whole model.

Figures 12a, 13a, and 14a show the 2D horizontal conductivity distributions inverted from the 2D crosshole data between holes C10-UT1, UT2-C10, and UT1-UT2, respectively. These are compared with the horizontal velocity distribution, the relative GPR amplitude, and the predicted porosity and permeability on the same

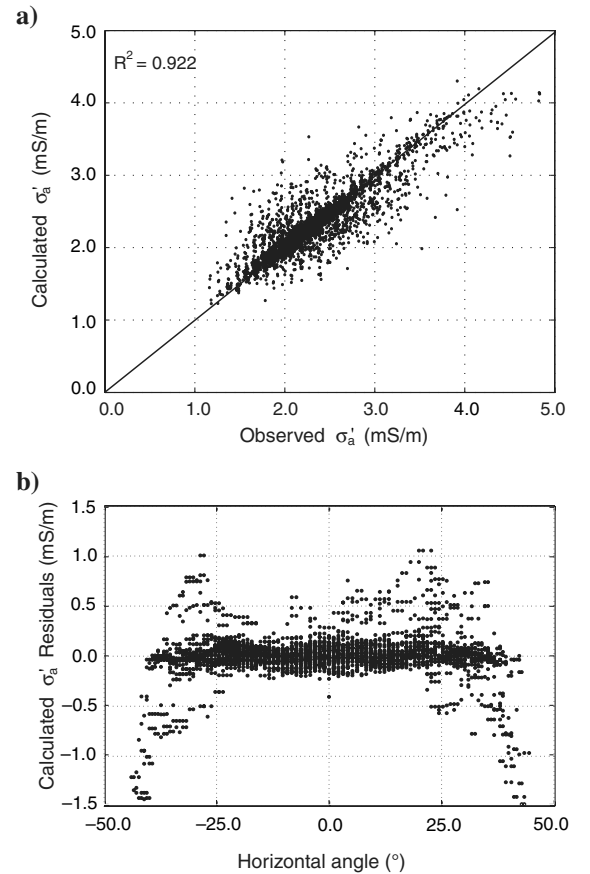


Figure 11. (a) Observed versus calculated apparent real conductivity from the 2D anisotropic conductivity tomography between holes UT1 and C10; data points for a perfect tomography solution would lie along the straight diagonal line. (b) The same data as in (a), but residuals are plotted as a function of propagation angle; positive angles correspond to a transmitter deeper than the receiver. In (b) the mean residual is -4.14×10^{-7} mS/m, and the standard deviation is 1.56×10^{-4} mS/m.

2D slices; the latter are all produced from the 3D surface GPR data (Harbi and McMechan, 2011). In Figures 12, 13, and 14, the solid and dashed black lines correlate the main features in the attribute sections; most of them are along fractures or layer boundaries. The subhorizontal dotted white lines delineate the two main facies boundaries in the volume; disturbed host rocks (facies 3) at the top, coarse- and fine-clast chaotic breccia facies (facies 4 and 5) in the middle, and coarse-clast chaotic breccia (facies 4) at the bottom (McMechan et al., 2002; Loucks et al., 2004; Harbi and McMechan, 2011). The largest interpreted faults, labeled 1 and 2 in Figures 12, 13, and 14, have northeast–southwest strikes, which is consistent with the regional Ouachita trend (Gale and Gomez, 2007). The interpretations are constrained mainly by the relative amplitudes (Figures 12c, 13c, and 14c); lines are included in the plots of the other attributes where they have modest to good correlation. Because tomography produces relatively low-resolution conductivity images, there is not a correlation with the finer-scale details, but rather with the larger-scale features, of the GPR and petrophysical attributes. The regions of differing conductivity tend to be bounded by the main lithologic boundaries, the GPR facies, and the larger fractures (the white dotted, and the black solid and dotted lines, respectively, in Figures 12, 13, and 14). The finer-scale breccias do not correlate at the low wavenumbers in the conductivity tomography images.

Higher conductivity values are at the tops of all three sections (Figures 12, 13, and 14), which is expected, because the study

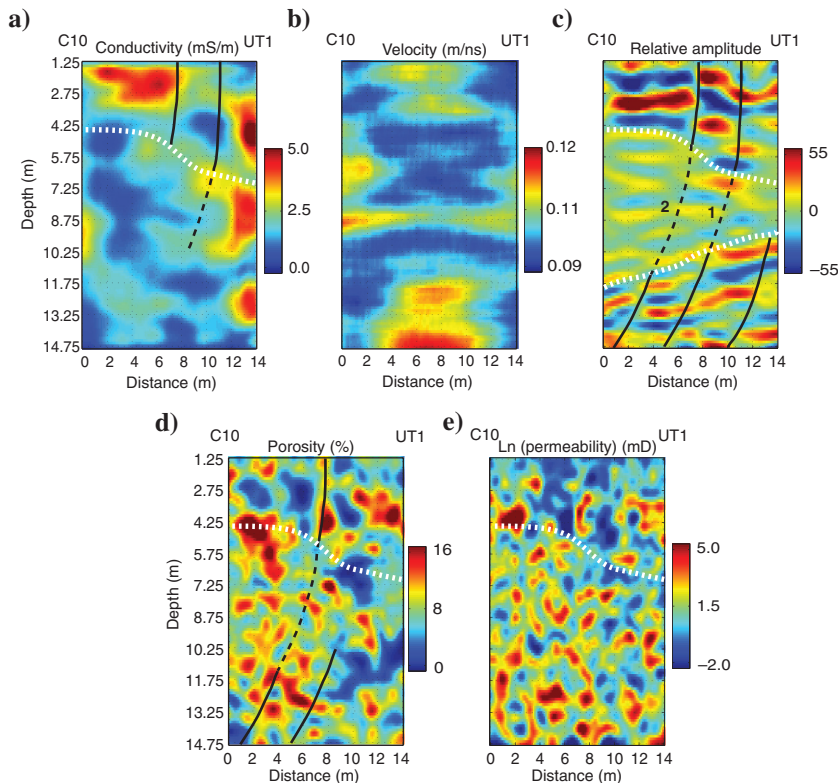


Figure 12. 2D vertical slices of (a) horizontal conductivity and (b) horizontal velocity between holes C10 (at 0.0 m) and UT1 (at 14.0 m). (c) is the relative GPR amplitude from the surface survey data (d) and (e) are the predicted porosity and permeability from Harbi and McMechan (2011). The grid increments are 0.25 m in vertical and horizontal directions. The black dashed and solid lines indicate interpreted faults that correlate between plots; the white dotted lines are the interpreted facies boundaries.

volume is above the water table and the only source of water is from the surface through fractures and the three open holes (the GPR tomography survey is acquired ~ 5 years after the holes are drilled). The estimated increase in conductivity near hole UT1 (Figures 12 and 14) is interpreted as being caused by penetration of surface water and a surface karst pit containing organic matter near the hole (Harbi and McMechan, 2011). Because of the high correlation of attenuation with water content (Davis and Annan, 1989), conductivity distributions follow the general structure imaged by the relative amplitudes (Figures 12c, 13c, and 14c), and thus with the predicted porosity and permeability (roughly bounded by the (dotted) facies lines in Figures 12, 13, and 14).

DISCUSSION

GPR attenuation is partially intrinsic (associated with the real conductivity and dielectric relaxation) and partially scattering (associated with the medium heterogeneity). For GPR, the contribution of σ' to intrinsic Q_{in}^{-1} is a function of frequency (Daniels, 1996). Scattering attenuation is also a function of frequency with maximum contribution at wavelengths close to the scatterer sizes (Frankel and Clayton, 1984; Tang and Burns, 1992; Kang and McMechan, 1994). Our workflow separates the intrinsic and scattering Q^{-1} in GPR data, estimates the conductivity and dielectric relaxation mechanism contributions to the intrinsic Q_{in}^{-1} , images the conductivity by tomography, and extracts the dominant scatterer

sizes from the wavenumber spectra of the scattered waves. Applications to synthetic and field crosshole data illustrate the procedures and results.

Separation of intrinsic and scattering Q^{-1} depends mostly on the accuracy of fitting the intrinsic attenuation, not whether the real conductivity or the dielectric relaxation has the dominant effect in intrinsic attenuation. Estimation of intrinsic conductivity is not affected by the relaxation magnitude as long the latter is independent of frequency. The absolute errors in the estimation of σ' (Table 2) are larger than those of ϵ''/ϵ' (Table 3) because the values of σ' are larger, but they are fairly constant within each group at fixed σ' or ϵ''/ϵ' (so the relative error increases with decreasing σ' and ϵ''/ϵ').

Scattering attenuation may locally distort the shape and magnitude of the Q_T^{-1} for all frequencies, which then may underestimate the scattering contribution and overestimate the relaxation effect, but still accurately estimate the real conductivity as the latter depends only on the dominant decay rate over frequency (not the absolute signal amplitude, the source strength, or local spectral deviations). For magnetic materials, magnetic relaxation also is assumed to be frequency-independent (Xu and McMechan, 1997), and thus also can easily be incorporated into the proposed methodology. This does not change the estimation of σ' , but it overlaps with the dielectric relaxation and it will be difficult to separate the two relaxation effects. Separation of Q_{in}^{-1} and Q_{sc}^{-1} is straightforward as long they

present different frequency dependence. If scatterers are in a continuous distribution of sizes over the same frequency range, this will be seen as a broad, smooth distribution in the wavenumber spectra (see Figure 5) (Frankel and Clayton, 1984). For a tighter wavenumber distribution, there are sidelobes of wavenumbers at multiples of the dominant wavenumber contribution, related to resonance in the scattering.

GPR amplitudes are controlled by many factors (Davis and Annan, 1989). Some of these can be approximated geometrically (including geometrical spreading, antenna sensitivity, and directivity) while others (such as antenna coupling), may not. In field data processing, we correct for the geometrical spreading and the antenna directivity, and assume all the other parameters are constant for each common-transmitter gather, as the transmitter position is fixed during acquisition of each. System performance and equipment drift is stable within each common-transmitter gather as each takes less than 5 minutes to record.

The formulation we use for scattering is a self-similar model, for lack of any specific information. If another model type was used, the results would be similar, but different. Clearly any auxiliary information that constrains the scatterer model will be beneficial in increasing the reliability of the estimates. The model also assumes only first-order scattering, but in fact, scattered waves become multiscattered and attenuated, and attenuated waves between scattered; it is an infinite series. This is a plausible explanation for the difference in the Q_t^{-1} curves for different conductivities in Figure 5, where higher conductivities clearly are associated with progressively smaller scattering amplitudes.

Estimating the transmitter wavefield spectrum is a critical step and is subject to accumulated errors from estimating the average intrinsic attenuation between holes, the receiver spectra calculation, and from using the air wave spectrum shape. However, conductivity estimation is more sensitive to the transmitter wavefield spectrum shape (it depends on the rate of decay as a function of frequency). In

data with a good signal-to-noise ratio, the best conductivity estimation is obtained from the best fit to the total Q_t^{-1} , which then gives the best scattering Q_{sc}^{-1} estimation and separation. In the current field data examples, the average real conductivities between the three pairs of holes are similar to those measured from the cores (~0.25 to 2.80 mS/m) (McMechan et al., 2002). Correlation between the current conductivity estimation and the measurements from core samples is not expected to be exact, as the GPR crosshole data acquisition is performed long after the core sample collection (2007 and 1999, respectively), and there will be scale differences between the core/lab and field GPR data (Guéguen and Palciauskas, 1994).

In the source estimation and the conductivity tomography, we use raypaths obtained by velocity tomography, based on single propagation trajectories. This is an assumption as the spectrum of the arriving waves is actually a superposition of multiple paths; while the spectrum may be dominated by the minimum-time signal, there is no guarantee that scattering does not play a role. We have tried to minimize this effect by windowing the pulse in time with a 40 ns window to reduce the coda contribution. Figure 11 shows the uncertainty associated with this (and all other factors not explicitly or accurately accounted for in the conductivity estimation). The conductivity correlation coefficient here (0.922) is smaller than that obtained by Harbi and McMechan (2011) for the times in the velocity tomography (0.9968); this difference is an indication of the upper bound on the magnitude of the uncertainties associated with the assumptions in the conductivity tomography.

For a homogenous velocity distribution, the velocity in the right side of equation 19 can be replaced with the average velocity along the rays that are used in calculating the real conductivity. Then, equation 19 reduces to

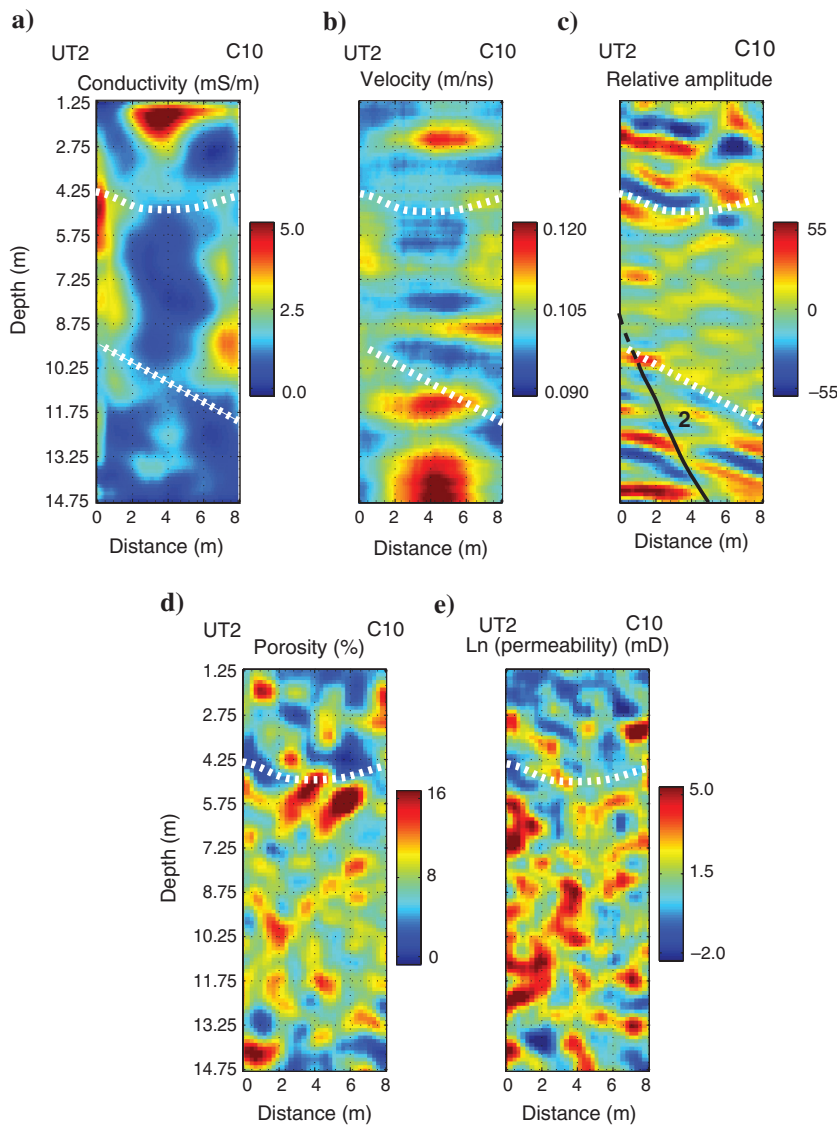


Figure 13. Similar representation to Figure 12 between holes UT2 at (0.0 m) and C10 at (8.0 m). The grid increments are 0.25 m in vertical and horizontal directions.

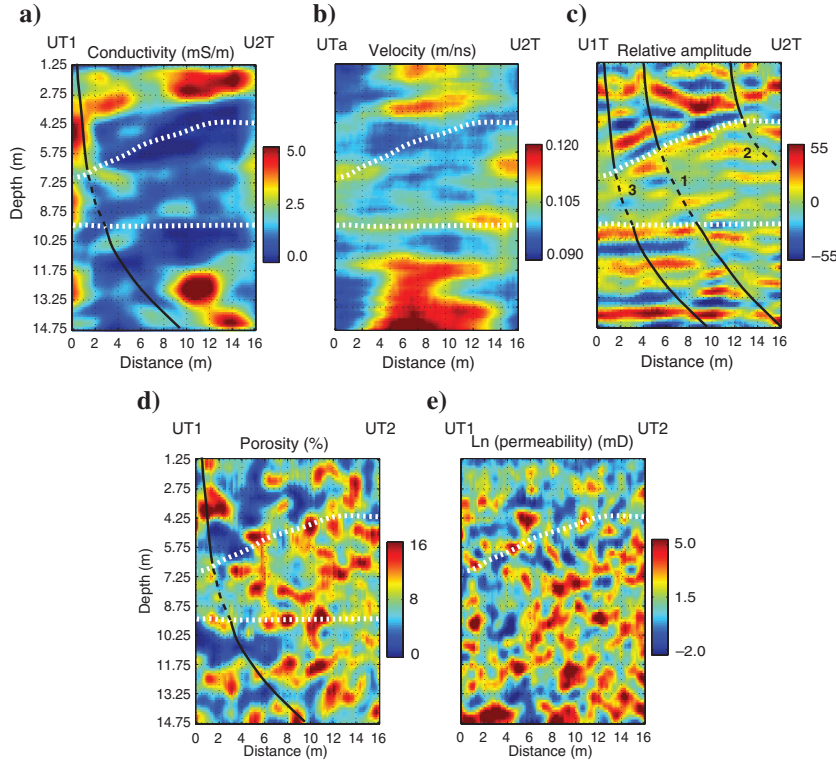


Figure 14. Similar representation to Figure 12 for between holes UT1 at (0.0 m) and UT2 at (16.0 m). The grid increments are 0.25 m in vertical and horizontal directions.

$$x\sigma'_a = \sum_{j=1}^m \sigma'_j dl_j \quad (24)$$

for $x\sigma'_a$ being the apparent real conductivity along the raypath of length x .

CONCLUSIONS

GPR scattering and intrinsic attenuation give different information about subsurface heterogeneities. Intrinsic attenuation (Q_{in}^{-1}) is a combination of two terms, the real conductivity effects ($\sigma'/\omega\epsilon'$) and the dielectric relaxation (ϵ''/ϵ') effects. At the frequencies $> \sim 40$ MHz in the present field data example, ϵ''/ϵ' is frequency-independent, and at frequencies less than ~ 200 MHz, $\sigma'/\omega\epsilon'$ is frequency-dependent for conductivities greater than ~ 1 mS/m. Each of the three components of Q_T^{-1} (Q_{sc}^{-1} and the two components of Q_{in}^{-1}) has its own frequency characteristic that allows their separation and estimation.

For synthetic and real crosshole GPR data, we estimate the total Q_T^{-1} as a function of frequency by the spectral ratio method, fit the real conductivity and dielectric relaxation to the intrinsic attenuation to determine the best-fit values, and then subtract the best-fitted intrinsic Q_{in}^{-1} from the total Q_T^{-1} to get the scattering attenuation Q_{sc}^{-1} contribution as a function of frequency. In a synthetic data test, the proposed procedure is shown to be robust, and estimates the real conductivity and permittivity relaxation with acceptable accuracy.

Between three pairs of holes in the Ellenburger reservoir analog, we separate and estimate the real conductivity, dielectric relaxation, and the scattering contributions from the total Q_T^{-1} . The estimated

real conductivity and dielectric relaxation values are well correlated with the lab measurements from core samples. Scattering contributions are used to image the breccia size spectra using the wavenumber relationship to the scatterer size ($KA = 1$ and $KA = 1.5$ for 2D and 3D models, respectively). The real attenuation values along raypaths are then input to anisotropic conductivity tomography. Although the tomography results are qualitatively consistent with the available information, more evaluative tests with synthetic data are needed to investigate its limitations. The low wavenumbers in the real conductivity distribution obtained by tomography generally follow the main GPR amplitude structure, the facies, and the larger fractures interpreted in a previous study by Harbi and McMechan.

ACKNOWLEDGMENTS

The research leading to this paper is supported by the sponsors of the UTD Geophysical Consortium. The FDTD code use in the synthetic example is from Xu and McMechan (2007). The core sample measurements and analysis are provided by a previous project funded by the Gas Research Institute under Contract 5097-210-3889. Tom Cook and Rick Hohman of Lhoist North America (formerly Chemical Lime Company), Marble Falls, TX allowed access to the field site and provided logistical support. Xiaoxian Zeng provided expert technical help in the field data acquisition. The surface and borehole PulseEKKO IV GPR systems are manufactured by Sensors & Software, Inc. The first author is also greatly indebted to King Abdulaziz University, Saudi Arabia, for their scholarship support. This paper is Contribution No. 1229 from the Geosciences Department at the University of Texas at Dallas.

REFERENCES

- Aki, K., and P. G. Richards, 1989, Quantitative seismology: Theory and methods: W. H. Freeman.
- Amthor, J., and G. Friedman, 1991, Dolomite-rock textures and secondary porosity development in Ellenburger group carbonates (Lower Ordovician), west Texas and southeastern New Mexico: *Sedimentology*, **38**, 343–362, doi: [10.1111/sed.1991.38.issue-2](https://doi.org/10.1111/sed.1991.38.issue-2).
- Annan, A. P., 1973, Radio interferometry depth sounding: Part I — Theoretical discussion: *Geophysics*, **38**, 557–580, doi: [10.1190/1.1440360](https://doi.org/10.1190/1.1440360).
- Annan, A. P., 1996, Transmission dispersion and GPR: *Journal of Environmental & Engineering Geophysics*, **0**, no. 2, 125–135.
- Arias-Castro, E., and D. L. Donoho, 2009, Does median filtering truly preserve edges better than linear filtering?: *Annals of statistics*, **37**, 1172–1206, doi: [10.1214/08-AOS604](https://doi.org/10.1214/08-AOS604).
- Bachrach, R., and T. Mukerji, 2005, Analysis of 3D high-resolution shallow seismic and crosswell GPR tomography for aquifer characterization: A case study, in D. K. Butler, ed., *Investigations in Geophysics, Near Surface Geophysics*: SEG, **13**, 607–619.
- Báth, M., 1974, Spectral analysis in geophysics: In development in solid earth geophysics: Elsevier Scientific Publishing Company.
- Behura, J., and I. Tsvankin, 2009, Estimation of interval anisotropic attenuation from reflection data: *Geophysics*, **74**, no. 6, A69–A74, doi: [10.1190/1.3191733](https://doi.org/10.1190/1.3191733).
- Bohidar, R., and J. Hermance, 2002, The GPR refraction method: *Geophysics*, **67**, 1474–1485, doi: [10.1190/1.1512792](https://doi.org/10.1190/1.1512792).
- Bradford, J. H., 2007, Frequency-dependent attenuation analysis of ground-penetrating radar data: *Geophysics*, **72**, no. 3, J7–J16, doi: [10.1190/1.2710183](https://doi.org/10.1190/1.2710183).

- Brzostowski, M. A., and G. A. McMechan, 1992, 3D tomographic imaging of near-surface seismic velocity and attenuation: *Geophysics*, **57**, 396–403, doi: [10.1190/1.1443254](https://doi.org/10.1190/1.1443254).
- Cai, J., and G. A. McMechan, 1995, Ray-based synthesis of bistatic ground-penetrating radar profiles: *Geophysics*, **60**, 87–96, doi: [10.1190/1.1443766](https://doi.org/10.1190/1.1443766).
- Cassidy, N. J., 2008, GPR attenuation and scattering in a mature hydrocarbon spill: A modeling study: *Vadose Zone Journal*, **7**, 140–159.
- Chang, H., and G. A. McMechan, 1996, Numerical simulation of multi-parameter seismic scattering: *Bulletin of the Seismological Society of America*, **86**, 1820–1829.
- Chang, P., D. Alumbaugh, J. Brainard, and L. Hall, 2004, The application of ground-penetrating radar attenuation tomography in a vadose zone infiltration experiment: *Journal of Contaminant Hydrology*, **71**, 67–87, doi: [10.1016/j.jconhyd.2003.09.011](https://doi.org/10.1016/j.jconhyd.2003.09.011).
- Cole, K. S., and R. S. Cole, 1941, Dispersion and absorption in dielectrics: I: Alternating current characteristics: *Journal of Chemical Physics*, **9**, 341–351.
- Crossley, D. J., and O. G. Jensen, 1989, Fractal velocity models in refraction seismology: *Pure and Applied Geophysics*, **131**, 61–76, doi: [10.1007/BF00874480](https://doi.org/10.1007/BF00874480).
- Dainty, A. M., 1981, A scattering model to explain seismic q observations in lithosphere between 1 and 30 Hz: *Geophysical Research Letters*, **8**, 1126–1128, doi: [10.1029/GL008i01p01126](https://doi.org/10.1029/GL008i01p01126).
- Daniels, D. J., 1996, *Surface-penetrating radar*: The Institution of Electrical Engineers.
- Dasios, A., T. Astin, and C. McCann, 2001, Compressional wave q-estimation from full-waveform sonic data: *Geophysical Prospecting*, **49**, no. 3, 353–373, doi: [10.1046/j.1365-2478.2001.00259.x](https://doi.org/10.1046/j.1365-2478.2001.00259.x).
- Davis, J. L., and A. P. Annan, 1989, Ground-penetrating radar for high-resolution mapping of soil and rock stratigraphy: *Geophysical Prospecting*, **37**, 531–551, doi: [10.1111/gpr.1989.37.issue-5](https://doi.org/10.1111/gpr.1989.37.issue-5).
- Debye, P., 1945, *Polar molecules*: Dover Publication Inc.
- Deiana, R., G. Cassiani, A. Villa, A. Bagliani, and V. Bruno, 2008, Calibration of a vadose zone model using water injection monitored by GPR and electrical resistivity tomography: *Vadose Zone Journal*, **7**, 215–226.
- Dines, K., and R. Lytle, 1979, Computerized geophysical tomography: *Proceedings of the IEEE*, **67**, 1065–1073, doi: [10.1109/PROC.1979.11390](https://doi.org/10.1109/PROC.1979.11390).
- Dobroka, M., L. Dresen, C. Gelbke, and H. Rüter, 1992, Tomographic inversion of normalized data: Double-trace tomography algorithms: *Geophysical Prospecting*, **40**, 1–14, doi: [10.1111/gpr.1992.40.issue-1](https://doi.org/10.1111/gpr.1992.40.issue-1).
- Fisher, E., G. A. McMechan, P. Annan, and S. Cosway, 1992a, Acquisition and processing of wide-aperture ground-penetrating radar data: *Geophysics*, **57**, 495–504, doi: [10.1190/1.1443265](https://doi.org/10.1190/1.1443265).
- Fisher, E., G. A. McMechan, P. Annan, and S. Cosway, 1992b, Examples of reverse-time migration of single-channel, ground-penetrating radar profiles: *Geophysics*, **57**, 577–586, doi: [10.1190/1.1443271](https://doi.org/10.1190/1.1443271).
- Frankel, A., and R. W. Clayton, 1984, A finite-difference simulation of wave propagation in two-dimensional random media: *Bulletin of the Seismological Society of America*, **74**, 2167–2186.
- Frankel, A., and R. W. Clayton, 1986, Finite difference simulations of seismic scattering: Implications for propagation of short-period waves in the crust and models of crustal heterogeneity: *Journal of Geophysical Research*, **91**, 6465–6489, doi: [10.1029/JB091B06p06465](https://doi.org/10.1029/JB091B06p06465).
- Frenje, H., and C. Juhlin, 2000, Scattering attenuation: 2D and 3D finite difference simulation vs. theory: *Journal of applied geophysics*, **44**, 33–46, doi: [10.1016/S0926-9851\(00\)00003-3](https://doi.org/10.1016/S0926-9851(00)00003-3).
- Gale, J., and L. Gomez, 2007, Late opening-mode fractures in karst-brecciated dolostones of the Lower Ordovician Ellenburger group, west Texas: Recognition, characterization, and implications for fluid flow: *AAPG Bulletin*, **91**, 1005–1023.
- Giampiccolo, E., T. Tuvé, S. Gresta, and D. Patané, 2006, S-waves attenuation and separation of scattering and intrinsic absorption of seismic energy in southeastern Sicily (Italy): *Geophysical Journal International*, **165**, 211–222, doi: [10.1111/gji.2006.165.issue-1](https://doi.org/10.1111/gji.2006.165.issue-1).
- Giroux, B., and M. Chouteau, 2004, The effect of clay seams in borehole GPR attenuation tomography: *Proceedings, 10th International Conference on Ground-Penetrating Radar*, Delft University of Technology, 221–224.
- Giroux, B., and M. Chouteau, 2010, Quantitative analysis of water-content estimation error using ground-penetrating radar data and a low-loss approximation: *Geophysics*, **75**, no. 4, WA241–WA249, doi: [10.1190/1.3464329](https://doi.org/10.1190/1.3464329).
- Greaves, R. J., D. P. Lesmes, J. M. Lee, and M. N. Toksöz, 1996, Velocity variation and water content estimated from multi-offset, ground-penetrating radar: *Geophysics*, **61**, 683–695, doi: [10.1190/1.1443996](https://doi.org/10.1190/1.1443996).
- Grimm, R. E., E. Heggy, S. Clifford, C. Dinwiddie, R. McGinnis, and D. Farrell, 2006, Absorption and scattering in ground-penetrating radar: Analysis of the Bishop Tuff: *Journal of Geophysical Research*, **111**, 1–15, doi: [10.1029/2005JE002619](https://doi.org/10.1029/2005JE002619).
- Guéguen, Y., and V. Palciauskas, 1994, *Introduction to the physics of rocks*: Princeton University Press.
- Hackert, C. L., and J. O. Parra, 2003, Estimating scattering attenuation from vugs or karsts: *Geophysics*, **68**, 1182–1188, doi: [10.1190/1.1598111](https://doi.org/10.1190/1.1598111).
- Hammon, W., III, X. Zeng, R. Corbeau, and G. A. McMechan, 2002, Estimation of the spatial distribution of fluid permeability from surface and tomographic GPR data and core, with a 2D example from the Ferron Sandstone, Utah: *Geophysics*, **67**, 1505–1515, doi: [10.1190/1.1512746](https://doi.org/10.1190/1.1512746).
- Hamstad, M. A., A. Ógallagher, and J. Gary, 2001, Effects of lateral plate dimension on acoustic emission signals from dipole source: *Journal of Acoustic Emission*, **19**, 258–274.
- Hanafy, S., and S. A. Hagrey, 2006, Ground-penetrating radar tomography for soil-moisture heterogeneity: *Geophysics*, **71**, no. 1, K9–K18, doi: [10.1190/1.2159052](https://doi.org/10.1190/1.2159052).
- Harbi, H., and G. A. McMechan, 2011, Modeling 3D porosity and permeability from GPR data in the Ellenburger Dolomite, central Texas: *Geophysics*, **76**, no. 6, J35–J46, doi: [10.1190/geo2011-0051.1](https://doi.org/10.1190/geo2011-0051.1).
- Hollender, F., S. Tillard, and L. Corin, 1999, Multifold borehole radar acquisition and processing: *Geophysical Prospecting*, **47**, 1077–1090.
- Holliger, K., and T. Bergmann, 2002, Numerical modeling of borehole georadar data: *Geophysics*, **67**, 1249–1257, doi: [10.1190/1.1500387](https://doi.org/10.1190/1.1500387).
- Holliger, K., M. Musil, and H. R. Maurer, 2001, Ray-based amplitude tomography for crosshole georadar data: *Journal of Applied Geophysics*, **47**, 285–298, doi: [10.1016/S0926-9851\(01\)00072-6](https://doi.org/10.1016/S0926-9851(01)00072-6).
- Irving, J. D., 2006, Improving tomographic estimates of subsurface electromagnetic wave velocity obtained from ground-penetrating radar data: Ph.D. dissertation, Stanford University.
- Jannsen, D., J. Voss, and F. Theilen, 1985, Comparison of methods to determine Q in shallow marine sediments from vertical reflection seismograms: *Geophysical Prospecting*, **33**, 479–497, doi: [10.1111/gpr.1985.33.issue-4](https://doi.org/10.1111/gpr.1985.33.issue-4).
- Kang, I. B., and G. A. McMechan, 1994, Separation of intrinsic and scattering Q based on frequency-dependent amplitude ratios of transmitted waves: *Journal of Geophysical Research*, **99**, 23,875–23,885, doi: [10.1029/94JB02472](https://doi.org/10.1029/94JB02472).
- Keller, G. V., 1987, Rock and minerals properties, in N. M. Nabighian, ed., *Electromagnetic methods in applied geophysics-theory*: SEG, 13–51.
- Kerans, C., 1988, Karst-controlled reservoir heterogeneity in Ellenburger group carbonates of west Texas: *American Association of Petroleum Geologists Bulletin*, **72**, 1160–1183.
- Klein, K., and J. C. Santamarina, 1997, Methods for broadband dielectric permittivity measurements (soil-water mixtures, 5 Hz to 13 GHz): *Geotechnical Testing Journal*, **20**, 168–178, doi: [10.1520/GTJ10736J](https://doi.org/10.1520/GTJ10736J).
- Kneib, G., and S. A. Shapiro, 1995, Visco-acoustic wave propagation in 2D random media and separation of absorption and scattering attenuation: *Geophysics*, **60**, 459–467, doi: [10.1190/1.1443783](https://doi.org/10.1190/1.1443783).
- Koesoemadinata, A. P., and G. A. McMechan, 2003, Correlations between seismic parameters, EM parameters, and petrophysical/petrological properties for sandstone and carbonate at low-water saturations: *Geophysics*, **68**, 870–883, doi: [10.1190/1.1581039](https://doi.org/10.1190/1.1581039).
- Kowalsky, M. B., S. Finsterle, J. Peterson, S. Hubbard, Y. Rubin, E. Majer, A. Ward, and G. Gee, 2005, Estimation of field-scale soil hydraulic and dielectric parameters through joint inversion of GPR and hydrological data: *Water Resources Research*, **41**, 1–19, doi: [10.1029/2005WR004237](https://doi.org/10.1029/2005WR004237).
- Lehmann, F., D. Boerner, K. Holliger, and A. Green, 2000, Multicomponent georadar data: Some important implications for data acquisition and processing: *Geophysics*, **65**, 1542–1552, doi: [10.1190/1.1444842](https://doi.org/10.1190/1.1444842).
- Liu, L., 2006, Fracture characterization using borehole radar: Numerical modeling: *Water, Air, and Soil Pollution: Focus*, **6**, 17–34.
- Liu, L., J. W. Lane, and Y. Quan, 1998, Radar attenuation tomography using the centroid frequency downshift method: *Journal of Applied Geophysics*, **40**, 105–116, doi: [10.1016/S0926-9851\(98\)00024-X](https://doi.org/10.1016/S0926-9851(98)00024-X).
- Loucks, R., and J. Anderson, 1985, Depositional facies, diagenetic terranes, and porosity development in Lower Ordovician Ellenburger dolomite, Puckett Field, west Texas, carbonate petroleum reservoirs: Springer-Verlag, 19–37.
- Loucks, R., P. Mescher, and G. A. McMechan, 1999, Architecture of a coalesced, collapsed-paleocave system in the Lower Ordovician Ellenburger group, Dean Word Quarry, Marble Falls, Texas: *Gas Research Institute Report*, 5097-210-3889.
- Loucks, R., P. Mescher, and G. A. McMechan, 2004, Three-dimensional architecture of a coalesced, collapsed-paleocave system in the Lower Ordovician Ellenburger Group, central Texas: *AAPG Bulletin*, **88**, 545–564.
- McMechan, G. A., J. M. Harris, and L. M. Anderson, 1987, Crosshole tomography for strongly variable media with applications to scale model data: *Bulletin of the Seismological Society of America*, **77**, 1945–1960.
- McMechan, G. A., R. Loucks, P. Mescher, and X. Zeng, 2002, Characterization of a coalesced, collapsed paleocave reservoir analog using GPR and well-core data: *Geophysics*, **67**, 1148–1158, doi: [10.1190/1.1500376](https://doi.org/10.1190/1.1500376).
- Neep, J. P., M. S. Sams, M. H. Worthington, and K. A. ÓHara-Dhand, 1996, Measurement of seismic attenuation from high-resolution crosshole data: *Geophysics*, **61**, 1175–1188, doi: [10.1190/1.1444037](https://doi.org/10.1190/1.1444037).
- Oldenborger, G., P. S. Routh, and M. D. Knoll, 2007, Model reliability for 3D electrical resistivity tomography: Application of the volume of

- investigation index to a time-lapse monitoring experiment: *Geophysics*, **72**, no. 4, F167–F175, doi: [10.1190/1.2732550](https://doi.org/10.1190/1.2732550).
- Olhoeft, G. R., and D. E. Capron, 1994, Petrophysical causes of electromagnetic dispersion: Proceedings, 5th International Conference on Ground-Penetrating Radar, Waterloo Centre for Groundwater Research, 145–152.
- Parkhomenko, E. I., 1967, *Electrical properties of rocks*: Plenum Press.
- Quan, Y., and J. M. Harris, 1997, Seismic attenuation tomography using the frequency shift method: *Geophysics*, **62**, 895–905, doi: [10.1190/1.1444197](https://doi.org/10.1190/1.1444197).
- Reppert, P., F. D. Morgan, and M. N. Toksöz, 2000, Dielectric constant determination using ground-penetrating radar reflection coefficients: *Journal of Applied Geophysics*, **43**, 189–197, doi: [10.1016/S0926-9851\(99\)00058-0](https://doi.org/10.1016/S0926-9851(99)00058-0).
- Richards, P. G., and W. Menke, 1983, The apparent attenuation of a scattering medium: *Bulletin of the Seismological Society of America*, **73**, 1005–1021.
- Rickett, J., 2007, Estimating attenuation and relative information content of amplitude and phase spectra: *Geophysics*, **72**, no. 1, R19–R27, doi: [10.1190/1.2399451](https://doi.org/10.1190/1.2399451).
- Sato, M., and R. Thierbach, 1991, Analysis of a borehole radar in cross-hole mode: *IEEE Transactions on Geoscience and Remote Sensing*, **29**, 899–904, doi: [10.1109/36.101368](https://doi.org/10.1109/36.101368).
- Schmalholz, J., H. Stoffregen, A. Kemna, and U. Yaramanci, 2004, Imaging water content distributions inside a lysimeter using GPR tomography: *Vadose Zone Journal*, **3**, 1106–1115.
- Taherian, M. R., W. E. Kenyon, and K. A. Safinya, 1990, Measurement of dielectric response of water-saturation rocks: *Geophysics*, **55**, 1530–1541, doi: [10.1190/1.1442804](https://doi.org/10.1190/1.1442804).
- Takahashi, K., J. Igel, and H. Preetz, 2011, Clutter modeling for ground-penetrating radar measurements in heterogeneous soils: *IEEE Journal of Selected Topics in Applied Earth Observations and Remote Sensing*, **4**, no. 4, 739–747.
- Tang, X., and D. R. Burns, 1992, Seismic scattering and velocity dispersion due to heterogeneous lithology: 11th Annual International Meeting, SEG, Expanded Abstract, 824–827.
- Tarif, P., and T. Bourbie, 1987, Experimental comparison between spectral ratio and rise time techniques for attenuation measurement: *Geophysical Prospecting*, **35**, 668–680, doi: [10.1111/gpr.1987.35.issue-6](https://doi.org/10.1111/gpr.1987.35.issue-6).
- Tonn, R., 1989, Comparison of seven methods for computation of Q: *Physics of the Earth and Planetary Interiors*, **55**, 259–268, doi: [10.1016/0031-9201\(89\)90074-5](https://doi.org/10.1016/0031-9201(89)90074-5).
- Tonn, R., 1991, The determination of the seismic quality factor Q from VSP data: A comparison of different computational methods: *Geophysical Prospecting*, **39**, 1–27, doi: [10.1111/gpr.1991.39.issue-1](https://doi.org/10.1111/gpr.1991.39.issue-1).
- Topp, G. C., J. Davis, and A. P. Annan, 1980, Electromagnetic determination of soil water content; measurements in coaxial transmission lines: *Water Resources Research*, **16**, 574–582, doi: [10.1029/WR016i003p00574](https://doi.org/10.1029/WR016i003p00574).
- Tronicke, J., K. Holliger, W. Barrash, and M. D. Knoll, 2004, Multivariate analysis of crosshole georadar velocity and attenuation tomography for aquifer zonation: *Water Resources Research*, **40**, 1–14, doi: [10.1029/2003WR002031](https://doi.org/10.1029/2003WR002031).
- Turner, G., and A. F. Siggins, 1994, Constant Q attenuation of subsurface radar pulses: *Geophysics*, **59**, 1192–1200, doi: [10.1190/1.1443677](https://doi.org/10.1190/1.1443677).
- Um, J., and C. Thurber, 1987, A fast algorithm for two-point seismic ray tracing: *Bulletin of the Seismological Society of America*, **77**, 972–986.
- von Hippel, A. R., 1954, *Dielectric and waves*: John Wiley & Sons, Inc.
- Wharton, R. P., G. A. Hazen, R. N. Rau, and D. L. Best, 1980, Electromagnetic propagation logging: Advance in technique and interpretation: 55th Annual Fall Technical Conference and Exhibition, SPE paper 9267.
- Williamson, P. R., 1991, A guide to the limit of resolution imposed by scattering in ray tomography: *Geophysics*, **56**, 202–207, doi: [10.1190/1.1443032](https://doi.org/10.1190/1.1443032).
- Won, I. J., 2011, Apparent conductivity (or resistivity), <http://www.geophex.com/resources/ApparentConductivity.pdf>, accessed 4 February, 2012.
- Xu, T., and G. A. McMechan, 1997, GPR attenuation and its numerical simulation in 2.5 dimensions: *Geophysics*, **62**, 403–414, doi: [10.1190/1.1444151](https://doi.org/10.1190/1.1444151).
- Yomogida, K., and R. Benites, 1996, Coda Q as a combination of scattering and intrinsic attenuation: Numerical simulations with the boundary integral method: *Pure and Applied Geophysics*, **148**, 255–268, doi: [10.1007/BF00882062](https://doi.org/10.1007/BF00882062).
- Zhou, B., and P. K. Fullagar, 2001, Delineation of sulphide ore-zones by borehole radar tomography at Hellyer Mine, Australia: *Journal of Applied Geophysics*, **47**, 261–269, doi: [10.1016/S0926-9851\(01\)00070-2](https://doi.org/10.1016/S0926-9851(01)00070-2).
- Zhou, C., L. Liu, and J. W. Lane Jr., 2001, Nonlinear inversion of borehole-radar tomography data to reconstruct velocity and attenuation distribution in earth materials: *Journal of Applied Geophysics*, **47**, 271–284, doi: [10.1016/S0926-9851\(01\)00071-4](https://doi.org/10.1016/S0926-9851(01)00071-4).
- Zhou, H., J. W. Lane, Jr., and M. Sato, 2005, Fracture imaging and saline tracer monitoring by crosshole borehole radar, in D. K. Butler, ed., *Near Surface Geophysics: Investigations in Geophysics*, no. 13, SEG, 563–571.
- Zhu, X., and G. A. McMechan, 1989, 2D tomographic imaging of velocities in the Wichita uplift-Anadarko basin region of southwestern Oklahoma: *Bulletin of the Seismological Society of America*, **79**, 873–887.